A Novel SAR Fractal Roughness Modeling of Complex Random Polar Media and Textural Synthesis Based on a Numerical Scattering Distribution Function Processing

Iman Heidarpour Shahrezaei and Hyun-Cheol Kim, *Member, IEEE*

***Abstract*—In this article, complex random polar media (CRPM) are synthesized by a forward numerical modeling based on the fractal statistical properties of the marginal ice zone (MIZ) in terms of its energy balance under sea state conditions. The proposed modeling was carried out by the parallel processing of a modified JONSWAP directional spectrum function in a two-dimensional hybrid domain. As a novel approach, the scattering formulation has been modified in the form of a two-scale implementation, which is optimized by the product of cosine-power and Gamma probability distribution function (PDF). As a result, a composite model of CRPM under different sea state conditions, including wind speed and direction, has been made possible. Due to the high dynamics of CRPM under sea state conditions, the presence of high entropy samples in the form of random roughness fluctuations is inevitable. These highly textured areas not only reduce the ability to resolve fine details but also make the interpretation difficult from a remote sensing point of view. According to the importance of synthetic aperture radar in the observation of MIZ and analysis of scattering properties, the spectral distribution modeling of these roughness anomalies and their electromagnetic interactions, along with surface tension synthesis, are presented here. Meanwhile, several objective quality metrics under different sea state conditions have been derived. The results show that the sea state not only changes the spectral components, but also affects their contribution to the roughness fluctuations and texture compositions. In short, this is for the first time that the composite modeling of CRPM based on directional spectrum function under sea state conditions along with electromagnetic interactions investigation and its pertinent texture analysis has been done.**

***Index Terms*—Composite directional spectrum function, numerical modeling, roughness, synthetic aperture radar (SAR), sea state.**

I. Introduction

SEA ice is a critical component of polar climate systems composed of ice sheets, which range in a horizontal scale from meters to many kilometers [1], [2]. These floes are particularly important for the marginal ice zone (MIZ), a spatially variable region separating open water from interior seasonal ice, where ocean surface waves can penetrate [3]. During the melt season, ocean waves are known to break up ice sheets and affect the extension of the MIZ, which would otherwise occur under quiescent freezing conditions [4], [5]. The ocean wave energy decays exponentially with the distance of propagation, and the rate is dependent on the frequency and thickness of the floe, which might cause the floe to bend in some parts or fracture in other areas [6]–[8]. As a result, small ice floes, in the form of a newly grown size category or the broken parts of old floes, are generated in the fetch, whereas ocean waves play an important role in their distribution and energy dissipation [1], [3], [9], [10]. In other words, as the incoming wave frequency alters, the energy scatters as the wave penetrates farther into the fetch. As a result, the MIZ constitutes an active region of dynamic interactions between ice floes and open water as well as the atmosphere, hereinafter referred to as complex random polar media (CRPM), which redistributes ocean wave energy and contributes to the formation of media [8], [9].

The analysis of this energy alteration phenomenon involves many complicated variables, and considerable idealization is required, which is a twofold mechanism [10]. The first is the wave-induced breaking of continuous ice and inelastic collisions in the form of a dissipative mechanism, and the second is a wave energy redistribution in the form of a CRPM scattering mechanism [11], [12]. The two mechanisms have different approaches, and the relative precedence of scattering and dissipative mechanisms in both the evolution of CRPM and the wave energy alterations is unclear; however, scattering tends to broaden the directional spread of the wavefield properties, whereas dissipation does not [13]. Accordingly, focusing on the wavefield properties of CRPM based on a scattering mechanism has been considered a suitable approach for studying the evolution of CRPM, which has been the focus of several studies [1]–[3], [5], [7], [12], [14]–[22].

In general, the scattering modeling of random media can be categorized into three areas: experimental methods, analytical models, and numerical simulations [23]. Despite the obvious limitations of experimental methods, much work has been devoted to understanding the validity domains of these approximations [24], [25]. Analytical scattering theories are of importance

Manuscript received March 16, 2021; revised April 28, 2021 and May 20, 2021; accepted May 26, 2021. Date of publication May 28, 2021; date of current version August 3, 2021. This work was supported by Korea Polar Research Institute under Grant PE21040 with the title of study on remote sensing for quantitative analysis of changes in the Arctic cryosphere. *(Corresponding author: Hyun-Cheol Kim.)*

Iman Heidarpour Shahrezaei is with the Center of Remote Sensing and GIS, Korea Polar Research Institute, Incheon 21990, South Korea (e-mail: i.heidarppour@kopri.re.kr).

Hyun-Cheol Kim is with the Center of Remote Sensing and GIS, Korea Polar Research Institute, Incheon 21990, South Korea (e-mail: kimhc@kopri.re.kr).

Digital Object Identifier 10.1109/JSTARS.2021.3084822

in modeling applications. They provide valuable insight into scattering properties and the physical behavior of surfaces. The main drawbacks of analytical models are the lack of domain categorization, the long computation time, and the scarce evaluation scenarios [26], [27]. To overcome the limitations of analytical modeling and to provide validation for experimental methods, numerical simulations have been proposed [23], [24], [28]–[32]. The bulk of numerical simulations in surface roughness modeling have been restricted to one-dimensional (1-D) surfaces relative to their mean direction, which makes them similar to the surface cross-section [4], [12], [14], [15], [20], [26], [28], [31], [33]. With the advent of computational processing and numerical techniques, attention has turned to 2-D or 3-D modeling of the surface [21], [22], [32], [34]–[36]. Since all numerical simulations are approximate, a tradeoff between accuracy, complexity, and dimensionality should be made in the modeling procedure [23]. More precisely, a numerical modeling remains well conditioned, as it follows the tradeoff in approximations and dimensionality [37], [38]. It is worth noting that other methods are exponentially unstable and only viable over a limited range of parameters that place them in the category of approximate methods [23].

Currently, both theoretical methods and numerical simulations are being applied to the study of physical phenomena that arise in ocean surface modeling that are inherently 2-D and cannot be observed using 1-D approximations, specifically while dealing with ocean waves known as sea state conditions [35], [36], [39]–[43]. Hence, characterizing the stochastic scattering properties of such nondeterministic complex media with a given statistical distribution of concentration and normal absorption data is considered a complicated approach to model ocean roughness [24], [42], [44], [45]. Accordingly, a numerical modeling of the MIZ under sea state conditions as an extreme ocean medium will not only be more complicated due to its complex structure but will also be a novel statistical scattering approach to visualize CRPM, which has not been reported in polar observations [1]–[3], [7]–[12], [16], [18], [19], [22], [36], [40]–[42], [44]–[49]. As an approach, CRPM surface roughness modeling is considered to be the scattering contribution of the physical state, the extent and dynamics of the MIZ based on its random distribution, and the concentration in terms of energy balance and its spectral characteristics under sea state conditions, which is of scientific importance in polar remote sensing [2]–[4], [8], [12], [13], [21], [22], [47]–[53].

To date, there is no published numerical surface modeling of CRPM and their relevant electromagnetic interactions or pertinent texture synthesis, although there is anecdotal evidence on the remote sensing interpretation of sea ice in the sense of synthetic aperture radar (SAR) applications [2], [4], [8], [12], [13], [21], [22], [40]–[43], [49]–[53]. It is worth noting that the majority of studies have focused on the physical formulation of solitary ice in the form of a dissipative layer floating on the surface of the ocean, but no studies have provided a proper model based on scattering properties under sea state conditions [2], [4], [7]–[9], [12], [13], [16], [18], [22], [23]–[25], [27]–[29], [31]–[37], [41], [42], [49]–[59]. In short, CRPM surface roughness modeling and the pertinent texture synthesis under sea state conditions, including wind speed alteration and direction deviation, is a novel concept that has yet to be reported [2], [4], [7], [9], [12]–[14], [16], [18], [19], [21], [22], [27], [29], [31], [35], [37]–[39], [46], [49], [58], [59]. Another advantage of such a texture visualization is the contribution of CRPM surface roughness to electromagnetic interactions, which play an important role in SAR sensor optimization, image formation algorithm development, image enhancement and identification, and reduce the need for experimental field observations [40]–[42], [46], [49]–[59].

To this end, a forward statistical modeling of CRPM based on the parallel processing of spectral distributions under sea state conditions is investigated in this research. The proposed numerical approach is mainly characterized by applying a modified version of the CRPM directional spectrum function in a 2-D hybrid domain [58], [60]–[63]. This modification addresses the parallel computation of the ice energy transfer function and its extraction based on an enhanced spreading function formulation [23], [60], [61]. This enhancement includes directional distribution function modification in the form of a cosine-power gamma PDF multiplied by an optimized distribution class under the control of the sea state [23], [53], [58], [62]. Accordingly, scattering properties are extracted in a domain whose frequency-dependent components have been assigned in compliance with the time-evolving sea state that affects the power spectral density (PSD) function of the entire surface of the CRPM [59], [64]–[67]. As an approach, the proposed numerical modeling has been modified in a composite manner known as a two-scale spectrum model, which includes both the high- and low-frequency components of the stochastic CRPM spectrum function under different scattering conditions of the sea state [23], [64], [65], [68], [69]. The proposed modeling covers major ocean wave modulation phenomena, including wideband resonant modulation impacts and narrowband filtering effects, which are determinative of the spectral distribution and surface roughness [23], [49], [53], [65], [67]–[69].

It is well known that for SAR image analysis of the polar region, precise knowledge of the surface evolution and the textural behavior of roughness are the prime requirements [2], [4], [12], [49]–[55], [59], [63], [70]. However, the embedded random roughness fluctuations and their resulting pixel anomalies play a significant role in the misinterpretation of such fractal analysis [49]–[55], [71], [72]. Hence, this study is not limited to CRPM modeling and has been extended to a fractal texture investigation of CRPM and their electromagnetic interactions as well as a surface tension synthesis in the presence of random roughness fluctuations. As another novel approach, an exponential polynomial (EP) probabilistic density formulation of random roughness fluctuations in terms of inherent texture anomalies has been adopted and evaluated under different sea state conditions [53], [65], [71]–[73].

To the best of authors' knowledge, this article takes a step toward the composite surface modeling of CRPM based on the parallel processing of scattering function modification under sea state conditions and investigates the fractal texture information, including roughness fluctuations, spectral distributions, electromagnetic interactions, and surface tension synthesis, which have not been reported altogether previously. In general, this work extends numerous studies [2], [10], [13], [23], [36], [41]–[43], [45], [49], [52], [53], [56]–[59], [61], [63], [70], [71], [73]–[79] that were only concerned with 1-D or 2-D formulations and

never addressed sea ice roughness modeling and the relevant textural evaluation. This evaluation includes the spectral property extraction of texture based on PSD modeling [53], [57] and an electromagnetic interaction investigation in terms of received backscattered data generation [59], [70], [72], [76], [80], as well as surface tension synthesis based on a tensor structure descriptor (TSD) field map [73]. The reference CRPM function is a modified two-scale JONSWAP directional spectrum function [79], which has been extended as a function of sea state for roughness modeling [61]. The proposed numerical modeling method reduces the reliance on 1-D approximations and empirical formulations of CRPM as well as other limitations associated with other surface roughness analyses, including dimensionality, large-scale formulation, coherent scattering effects, random geometry, and wavenumber complexities [1]–[14], [23], [51]–[55], [57]–[64], [67], [70], [74], [76]–[80]. The results have applications to polar remote sensing and SAR sea ice image interpretation in terms of ice concentration calculations, temperature profile derivations, polar radiometry applications, sensor optimizations, etc.

This article is organized as follows. Section II presents the CRPM modeling concept, formulation modifications, and surface roughness simulation results. This section also includes freeboard profile extractions under different sea state conditions. This section also introduces a 2-D directional distribution function evaluation of the reference two-scale spectrum of CRPM and the inherent highly textured area. In Section III, the resulting CRPM textures are evaluated based on roughness fluctuations, SAR electromagnetic interactions, and surface tension synthesis. A highly textured area formulation, based on EP distribution, raw data generation (RDG) and a TSD field map, is presented in this section. In Section IV, a series of objective quality assessment metrics are conducted to verify the whole roughness modeling procedure. Finally, Section V concludes this article.

II. CRPM Surface Roughness Modeling Approach

The basis of the MIZ directional spectrum function and its energy balance while ocean waves are scattered within the fetch has been studied [61], [65]–[67]. Apart from modifications to the existing theory and its typical 1-D or 2-D experiments, such as uniform floating plate formulas, the proposed statistical surface modeling of CRPM as a function of the sea state is a novel concept that has yet to be reported. To this end, the directional spectrum function of MIZ, in compliance with the JONSWAP energy balances, is the prime requirement. Accordingly, a forward numerical computation of the stochastic scattering properties of CRPM based on the JONSWAP function in contribution to the sea state will be discussed here. These results will help extract the freeboard profile and upgrade the scattering behavior information of a fetch under sea state conditions.

A. CRPM Energy Balance Formulation

The linearized wavenumber formulation of ocean waves under nonlinear boundary conditions, comprising superimposed regular cosine waves with random amplitudes, directions, and phases, can be stated as

$$\eta\ (r,t) = \ a\cos\left(\boldsymbol{k}.r - \omega t + \varphi\right) \tag{1}$$

where r is the horizontal distance, t is time, $\boldsymbol{k}$ is the wavenumber, a is the amplitude, φ is the initial angle of wave component, and ω is the angular frequency that can be determined from the dispersion relation as

$$\sigma\ (k) = \ 2\pi f = \sqrt{gk\tanh\left(kh\right)} \tag{2}$$

where h is the ocean depth, g is the gravitational constant, $\boldsymbol{k}/k$ is the direction of the traveling wave, and the wavelengths are $2\pi/k$ and $k = |\boldsymbol{k}|$. The phase angle ϕ in (1) defines the displacement at traveling time t but does not affect any of the physical properties of the wave. Since the equation is linear, the sum of waves can be expressed as

$$\eta\ (r,t) = \sum_{n=1}^{N} a_n \cos\left(\boldsymbol{k}_n.r_n - \omega_n t + \varphi_n\right),\ \omega_n = \sigma\left(k_n\right) \tag{3}$$

By assuming the independent and uniform phase distribution of φ_n, the expectation $\mathbb{E}$, and the variance $\mathbb{v}$, the ocean wave can then be obtained as

$$\begin{aligned} &\mathbb{E}\left(\eta\left(r,t\right)\right) = 0 \\ &\mathbb{v}\left(\eta\left(r,t\right)\right) = E\ \left(\eta^2\left(r,t\right)\right) = \sum_{n=1}^{N} \frac{a_n^2}{2} \end{aligned} \tag{4}$$

Subsequently, the primitive spectrum function of (3) with the help of the Dirac function can be introduced as

$$\Psi\ \left(\boldsymbol{k}\right) = \sum_{n=1}^{N} \frac{a_n^2}{2} \delta\left(\boldsymbol{k} - \boldsymbol{k}_n\right) \tag{5}$$

where Ψ contains the information about η as

$$\mathbb{v}\ \left(\eta\left(r,t\right)\right) = \int_{\boldsymbol{k}} \Psi\left(\boldsymbol{k}\right) d\boldsymbol{k} \tag{6}$$

Subsequently, instead of a finite number of waves, a continuous collection of waves in the form of $\Psi(\boldsymbol{k})$ can be considered. The corresponding function of Ψ is called the wavenumber spectrum, which defines a wave's scattering direction and wavelength by means of the dispersion frequency. The dispersion relation in (2) connects $\boldsymbol{k}$ and ω, which facilitates the application of directions θ_n and ω_n instead of $\boldsymbol{k}_n$. Accordingly, the polar transformation of the proposed wavenumber formulation can be substituted by its frequency and direction as

$$\begin{aligned} \int_{\boldsymbol{k}} \Psi\left(\boldsymbol{k}\right) d\boldsymbol{k} &= \int_{k=0}^{\infty} \int_{\theta=0}^{2\pi} \Psi\left(k,\theta\right) k\ dkd\theta \\ &= \int_{\omega=0}^{\infty} \int_{\theta=0}^{2\pi} \Psi\left(k\left(\omega\right),\theta\right)\ k\left(\omega\right) \frac{dk}{d\omega}\ d\omega d\theta \end{aligned} \tag{7}$$

where the wavenumber spectrum in terms of angular frequency ω and direction θ is called the directional wave spectrum as

$$F\ \left(\omega,\theta\right) = \ \Psi\left(k\left(\omega\right),\theta\right) k\left(\omega\right)\ \frac{dk\left(\omega\right)}{d\omega} = \ \Psi\left(k\left(\omega\right),\theta\right) \frac{k\left(\omega\right)}{v_g\left(k\right)} \tag{8}$$

where $v_g = \frac{\partial\omega}{\partial k}$ is the group velocity of waves. Accordingly, the directional spectrum function of the ocean, i.e., $F(\omega,\theta)$, can further be split into a product of

$$F\ \left(\omega,\theta\right) = \ S\left(\omega\right)\ D\left(\theta,\omega\right)\ N\left(\omega\right) \tag{9}$$

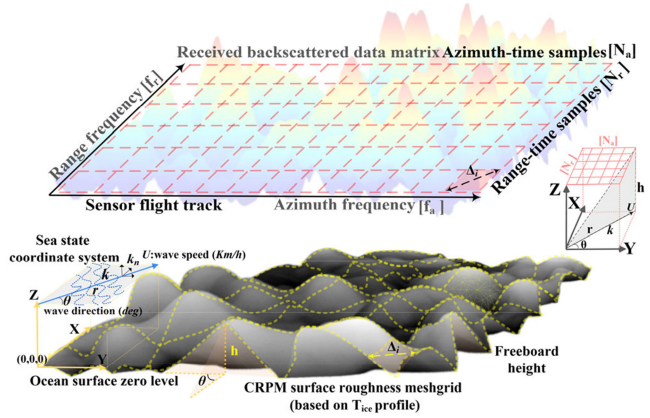

Fig. 1. CRPM boundary configurations and raw data backscattering geometry for composite roughness modeling.

where the angular dependent part $D(\theta,\omega)$ is called the directional distribution function, which is a function of the sea state, and $N(\omega)$ is the power normalization function known as the distribution class that not only affects the wave distribution but also modifies its energy balance. $S(\omega)$ is called the energy spectrum and contains all significant scattering components at both small and intermediate scales of spatial frequencies, which makes the spectrum similar to a two-scale or composite model as follows:

$$S\ (\omega) = S_l\ (\omega) + S_h\,(\omega) \tag{10}$$

where S_l is the low-frequency component and S_h is the high-frequency component of the spectrum that includes short and medium scales of wave, which are responsive to the sea state [65], [75], [77], [79]. Accordingly, $S(\omega)$ contains different energy components that respond nearly instantly to the sea state in the shape of capillary, gravity, and capillary–gravity wave scatterings. In other words, the proposed two-scale spectrum function in (10) is an omnidirectional spectrum that presents the spectral information of progressive waves in terms of energy dispersions [65]. Accordingly, every peak in the composite spectrum around $\boldsymbol{k} = k_{\rm n}$ indicates the contribution of waves in the direction of $k_{\rm n}$ that corresponds to the spectral regime of the ocean in the form of modulation effects, which modify the wave scatterings and intrinsic statistical roughness [53]. Since there is a direct correspondence between ω and k, it is possible to go back and forth between F and Ψ and extend the omnidirectional spectrum to the whole ocean regime. Accordingly, the composite scattering formulation of (9) can evolve in time t and space r based on the energy balance equation as [10], [64]

$$\frac{\partial F\,(\omega,\theta;r,t)}{\partial t} + v_g\,(\omega,\theta)\,.\nabla F\ (\omega,\theta;r,t) = S_{\rm in}\ + S_{\rm mo} + S_{\rm co} \tag{11}$$

where $S_{\rm in}$ is the input energy component of the sea state, $S_{\rm mo}$ is the intermodulation and dispersion energy component, and $S_{\rm co}$ is the coupling component due to nonlinear interactions among other energy components, including the intramodulations. In the case of CRPM and due to the complexity of the structure in the presence of ice floes, as shown in Fig. 1, the energy balance equation in (11) must be modified in a way that considers the effects of ice floes on the ocean wavefields [61], [65]. Since progressive waves can be neither generated nor dissipated by the usual breaking mechanism in that spectrum fraction ω_n of the ocean surface covered by ice, both $S_{\rm in}$ and $S_{\rm mo}$ are reduced by a factor of $(1-\omega_n)$ in (11). On the other hand, a new term of the energy component corresponding to ice floes $S_{\rm ice}$ that presents the average ocean wavefield dispersion due to its random presence within the CRPM will be added to (11). Hence, the modified scattering version of the energy balance in (11) takes the form of (12) for CRPM as [61]

$$\frac{dF_{\rm CRPM}\,(\omega,\theta;t)}{dt} = (S_{\rm in} + S_{\rm mo})\ (1-\omega_n) + S_{\rm co} + S_{\rm ice} \tag{12}$$

where the scattered spectrum of the CRPM can be obtained by summing each energy component based on wave contributions of the same frequency ω_i from all directions [62]. However, to simplify the surface modeling of CRPM, the medium is assumed to be in an unbounded condition that reduces the equation into the form of pure time-dependent scattering due to the elimination of the advective term of $v_g.\nabla F$ [61]. Hence, at each time step and for each frequency ω_n, the forward numerical component of the scattered spectrum $F^S_{\rm CRPM}$ proceeds with a first-order time difference integration under a particular sea state condition, whereas $S_{\rm ice}$ is introduced in the form of the ice transfer function as [61], [62]

$$\begin{aligned} F^S_{\rm CRPM}\ (\omega_n,\theta;t+\Delta t) = &\left[F^S_{\rm CRPM}\,(\omega_n,\theta;t)\right. \\ &\left.+\left((S_{\rm in}+S_{\rm mo})\,(1-\omega_n)+S_{\rm co}\right)\Delta t\right]\ [\boldsymbol{T}_{\rm ice}]_{\omega_n} \end{aligned} \tag{13}$$

As an approach, with the help of the reference CRPM energy spectrum $F_{\rm CRPM}$, for each frequency ω_n and the scattered CRPM wavefield, i.e., $F^S_{\rm CRPM}$, the transfer function of ice $[\boldsymbol{T}_{\rm ice}]_{\omega_n}$ or simply the ice energy component is obtained by the linear time-invariant convolutional product of the scattered spectrum and the reference function as [61]

$$[\boldsymbol{T}_{\rm ice}]_{\omega_n} = F^S_{\rm CRPM}\ (\omega_n,\theta;t_n) * F_{\rm CRPM}\,(\omega_n,\theta;t_n) \tag{14}$$

where the ice transfer function $[\boldsymbol{T}_{\rm ice}]_{\omega_n}$ has random scattering characteristics with a random distribution that is under the control of the sea state [61]. In other words, the roughness of ice floes on the basis of $\boldsymbol{T}_{\rm ice}$ profile is an unbounded probability distribution of samples with random statistics that has no preferred shape or orientation, as shown in Fig. 1. It is worth noting that both the directional distribution function and the reference composite spectrum play an important role in the energy balance of CRPM and the roughness modeling. In this research, the reference wavefield is assumed to follow the JONSWAP spectrum, while the directional distribution function is designed to be a gamma function, which is multiplied by an optimized normalization function as [62], [67]

$$\begin{aligned} F_{\rm CRPM}\ (\omega,\theta) = &\frac{\alpha g^2}{(2\pi)^4}\,\omega^{-5}\exp\left[-\frac{5}{4}\left(\frac{\omega}{\omega_p}\right)^{-4}\right] \\ &\times\gamma^{\exp\left[\frac{(\omega-\omega_p)^2}{2\varepsilon^2\omega_p^2}\right]} D\,(\omega,\theta)\,N\,(\omega) \end{aligned} \tag{15}$$

where

$$\varepsilon = \begin{cases} 0.07 & \text{for } \omega \le \omega_p \\ 0.09 & \text{for } \omega > \omega_p \end{cases} \tag{16}$$

where γ is the peak enhancement factor, ω_p is the peak frequency radiance, and α is the time-dependent constant, which

is derived as

$$\alpha = 0.033\left(\frac{{\omega_p}^2 U}{g}\right)^{\frac{2}{3}} \tag{17}$$

where U is the specified wind speed. Accordingly, the product of directional distribution function $D(\omega,\theta)$ and normalization function $N(\omega)$ is called the spreading function, which is designed to be a mix of the cosine-power and gamma PDF that is multiplied by the freeboard improvement factor as

$$D\left(\omega,\theta\right)N\ \left(\omega\right) = \ \xi cos^{2n}\left(\frac{\theta}{2}\right)\frac{2^{2n-1}\Gamma^2\left(n+1\right)}{\pi\Gamma\left(2n+1\right)} \tag{18}$$

where ξ is the optimization factor, which acts as a linear interpolator for freeboard value smoothing and

$$n = 10^{0.99}\left(\frac{\omega}{\omega_p}\right)^k$$

$$k = \begin{cases} 4.06 & \text{for } \omega \le \omega_p \\ -2.34 & \text{for } \omega > \omega_p \end{cases} \tag{19}$$

The proposed CRPM surface roughness modeling is designed to be a parallel processing of $\boldsymbol{T}_{\rm ice}$ extraction in the shape of sparse floe distribution, which allows the ocean wave scattering to follow the pattern of the JONSWAP spectrum as a function of sea state, including the wind speed and direction. The whole procedure of $\boldsymbol{T}_{\rm ice}$ profile extraction within the proposed framework of (14) is similar to the match filter response of a radar system, which deals with an incoming spectrum and the scattered response [72].

B. CRPM Surface Modeling Procedure

The proposed scattering formulation of the CRPM in Section II-A tends to decrease the energy content of the reference function $F_{\rm CRPM}$ and, more importantly, spread out the energy over a broader range of directions based on the sea state. In other words, the scattered energy spectrum $F^{\rm S}_{\rm CRPM}$ will be slightly diminished by dissipative processes that can affect the ice spectral energy redistribution. More specifically, each mass of floating ice dissipates and redistributes the energy balance as a function of the sea state. Hence, an energy dissipation computation based on scattered spectrum categorization is necessary for the purpose of surface modeling. As stated in (13), the energy dissipation is assumed to be divided into four major components. The first is the input energy component identical to the reference energy but of attenuated magnitudes in terms of $S_{\rm in}$ [79]

$$S_{\rm in}\ (\omega,\theta) = \begin{cases} 0 & \text{if } \left(\frac{U\cos\theta}{v_p}-1\right) < 0 \\ 0.25\frac{\rho_a}{\rho_o}\left(\frac{U\cos\theta}{v_p}-1\right)\omega F_{\rm CRPM}\left(\omega,\theta\right) & \text{otherwise} \end{cases} \tag{20}$$

where ρ_a and ρ_o are the densities of the atmosphere and ocean, and v_p is the phase velocity. The second is the intermodulation and energy dispersion components in terms of $S_{\rm mo}$, which follows (21):

$$S_{\rm mo}\ (\omega,\theta) = \ -C_d\bar{\omega}\left(\frac{\omega}{\bar{\omega}}\right)^2\left(\frac{\hat{\alpha}}{\hat{\alpha}_{PM}}\right)F_{\rm CRPM}\left(\omega,\theta\right) \tag{21}$$

where C_d is the dissipation constant and $\hat{\alpha}$ is the integral wave-steepness parameter as [79]

$$\hat{\alpha} = \frac{E\bar{\omega}^4}{g^2} \tag{22}$$

$$\bar{\omega} = E^{-1}\int_0^\infty\int_0^{2\pi} F_{\rm CRPM}\left(\omega,\theta\right)\omega\ d\omega d\theta \tag{23}$$

$$E = \int_0^\infty\int_0^{2\pi} F_{\rm CRPM}\left(\omega,\theta\right)\ d\omega d\theta \tag{24}$$

where the parameter $\hat{\alpha}_{\rm PM}$ is an experimental value [65], [79]. In other words, the intermodulation components are quasi-linear and proportional to the square of the frequency, with a coefficient that depends on spectral integration. The third component is the energy coupling due to nonlinear interactions of components associated with the superposition of coherent traveling waves in the back and forth directions. These nonlinear scatterings represent the energy exchange between components as they interact among themselves. This type of energy transmission is weak, but are important to the evolution of the MIZ. Due to their resonant characteristics, $S_{\rm co}$ is given by the Boltzmann integral as [10], [65], [79]

$$\frac{\partial S_{\rm co}}{\partial t} = \int\int\int G\left(\boldsymbol{k}_n\right)\delta_{\boldsymbol{k}}\delta_\omega f\left(\boldsymbol{k}_n\right)d\boldsymbol{k} \tag{25}$$

where $f(\boldsymbol{k}_n)$ is the action density function of wavenumber $\boldsymbol{k}_n$, $G(\boldsymbol{k}_n)$ is the coupling effect function and $\delta_{\boldsymbol{k}}$ and δ_ω are delta functions that represent the resonance conditions for wavenumber and frequency. The fourth is the directional scattering component of the reference function in the presence of ice that spreads out over all directions with the magnitude apportioned to $S_{\rm ice}$. The transformation of its energy spectrum depends on the directional characteristics of the sea state. In this study, modifications were properly made in the referenced JONSWAP function of (15) in a way that follows the distribution pattern of (18), which complies with the small and medium scales of the sea state, including capillary, gravity, and capillary–gravity waves known as progressive waves [61], [77], [79]. Accordingly, $\boldsymbol{T}_{\rm ice}$ profile extraction, as the energy scattering distribution of floes, can be used as a criterion for CRPM roughness modeling.

To this end, after initial boundary settings and appropriate domain transformation, the scattered energies of $F^{\rm S}_{CRPM}$ can be computed by the parallel superposition of each energy component based on sea state conditions and for all frequencies. In this study, all ocean waves are assumed to be intimately coupled, and the presence of discrete ice floes will homogenously affect the $F^{\rm S}_{\rm CRPM}$ properties of the same frequency simultaneously. Hence, for each frequency ω_n, the ice transfer function $[\boldsymbol{T}_{\rm ice}]_{\omega_n}$ can be concurrently obtained by (14), which is the correlation process of the reference spectrum $F_{\rm CRPM}(\omega_n,\theta)$ and the scattered spectrum $F^{\rm S}_{\rm CRPM}(\omega_n,\theta)$. The whole computation procedure is based on a parallel processing method that provides a faster computation of $\boldsymbol{T}_{\rm ice}$. Finally, after deriving an ensemble of scattered $\boldsymbol{T}_{\rm ice}$ samples for all frequencies, by means of a discrete Fourier transform, a subsequent 2-D fast Fourier transform (FFT), multiplying by the square root of the PSD and then applying the 2-D inverse FFT, a set of composite roughness values for the normalized CRPM will be generated.

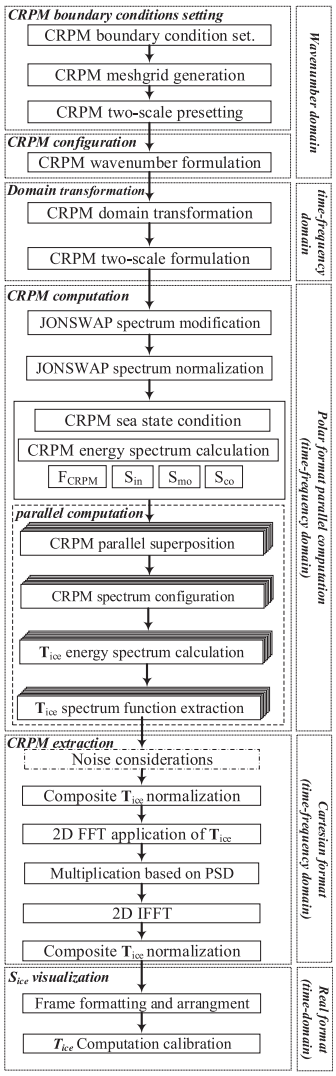

Fig. 2. CRPM surface roughness modeling algorithm.

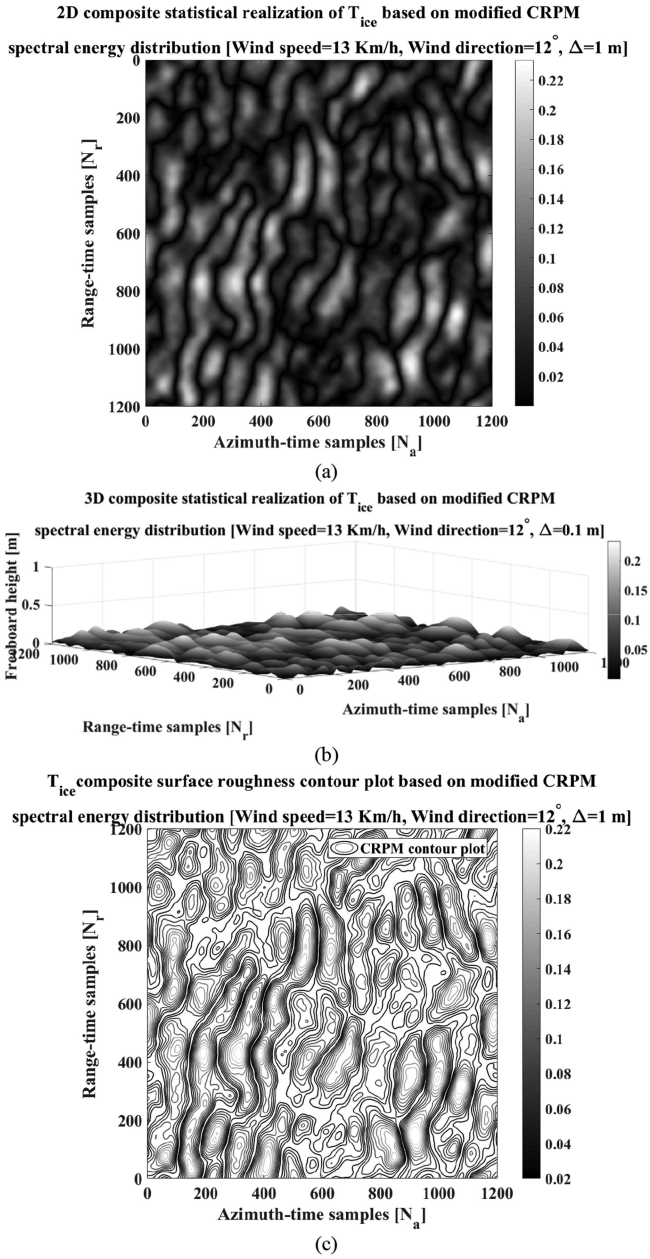

Fig. 3. CRPM roughness under the reference sea state conditions of wind speed = 13 km/h, $\theta = 12^{\circ}$, $\Delta = 0.$ m. (a) 2-D. (b) 3-D. (c) Contour plot.

Eventually, all these samples are frame formatted and integrated on a 2-D grid configuration based on the geometry in Fig. 1. This integration procedure is repeated for a series of time steps until the dominant trend of the CRPM can be established. It should be noted that at each computational time step, all the energy components are computed to obtain a new energy spectrum for each ω_n [23], [61], [65]. Thus, the PDF normalization of the JONSWAP spectrum plays an important role in an optimized modeling of CRPM due to values fluctuations. The surface roughness directly impacts the corresponding PSD behavior over the entire surface of the CRPM and vice versa. The whole modeling procedure of CRPM is presented in Fig. 2.

It should be noted that under the same sea state conditions, the computational complexity becomes more significant as the ratio of the mean roughness variance to the wavelength increases. In other words, the resolution of the surface has a direct impact on the roughness modeling. It is also worth noting that the fraction of floes within the CRPM affects the spectrum energy balance in (13).

Thus, the ice coverage is considered to be approximately half of the entire terrain, which is not only close to the real scenario but also suitable for the extraction of scattering profiles [77], [79]. According to the geometry in Fig. 1 and the modeling procedure in Fig. 2, the surface roughness under the presumed sea state condition with a wind speed of 13 km/h, direction of 12°, and 0.1 m resolution in an area of 120 m $\times$ 120 m under an optimized gamma distribution is presented in Fig. 3. The result in Fig. 3(a) shows the 2-D surface roughness presentation of the CRPM, where the black pixels represent the ocean surface and white pixels represent the ice distribution over the entire medium at both small and medium scales under sea state conditions.

Accordingly, the magnitude profile represents the height from the ocean zero level known as freeboard height.

As seen in Fig. 3(a) and (b), the maximum freeboard is derived as 0.2334 m and the minimum value is 0.11 m, while the average mean height is approximately 0.17 1 m. In comparison to the mean height of the freeboard, these minimum values can be considered minor intramodulation effects of wave couplings that relatively change based on the sea state in the form of small-scale roughness fluctuations. Due to the homogenous texture of ice floes on the one hand and the rapid small-scale fluctuations on the other hand, these statistical roughness alterations are determined to be surface zero levels or transitional edges between the ice and the ocean. In short, the proposed CRPM energy spectrum in (13) not only contributes to the random statistical distribution of ice floes in terms of $\boldsymbol{T}_{\mathrm{ice}}$ but also contributes to their shape and orientation based on boundary conditions. To further verify the proposed modeling, the above-mentioned scenario has been carried out under the same sea state conditions and a wider area with a tenfold increase in size of 1.2 km $\times$ 1.2 km in conjunction with a coarser resolution of up to ten times as 1 m. As shown in Fig. 4(a) and (b), the maximum freeboard height is derived to be approximately 0.2344 m, and the minimum value is 0.094 m, while the mean average height is calculated to be 0.15 2 m. It can be deduced that the difference in the freeboard profile is due to terrain extension and resolution degradation by a factor of 10, which makes the boundary conditions and the energy scatterings different from the results in Fig. 3.

Hence, under the same sea state conditions and different terrain parameters, the surface roughness profile will have almost the same maximum freeboard height but with different roughness details that are compared in Fig. 5. The azimuth direction has a slightly higher sensitivity to roughness alterations than the range while there is no particular pattern of such frictions on the modeling. In other words, under the presumed sea state and the designated boundary conditions, the increase in the resolution value would result in the reduction of samples per resolution cell. Under this condition, the probability of having heterogeneous surfaces with one or a few predominant scatterers increases, whereas the probability of having many diffusers decreases. In short, random roughness fluctuations of the CRPM result from energy scatterings of composite components under the presumed boundary conditions, whereas the terrain parameters will only affect the magnitudes. It should be noted that time steps are set to be small enough for rapid spectrum change detection, and the frequencies are adjusted independently. Therefore, it is necessary to analyze the effects of ocean momentum on the CRPM modeling. To this end, a surface roughness investigation based on the sea state, including wind speed alteration and direction deviation, was carried out on the reference image in Fig. 3, with a size of 120 $\mathrm{m}\times$ 120 m and a resolution of 0.1 m. As seen from the results in Figs. 6 and 7, changes in the sea state, whether the speed alteration or deviation in the direction, have a direct impact on the freeboard height profile and the embedded fluctuations, whereas no sea state condition outperforms the other. Similar to Fig. 5, the azimuth direction is more sensitive to roughness fluctuations than the range while no specific pattern is observed for their presence.

More specifically, neither the static nor the kinetic frictions of the CRPM surface in the form of freeboard height and its

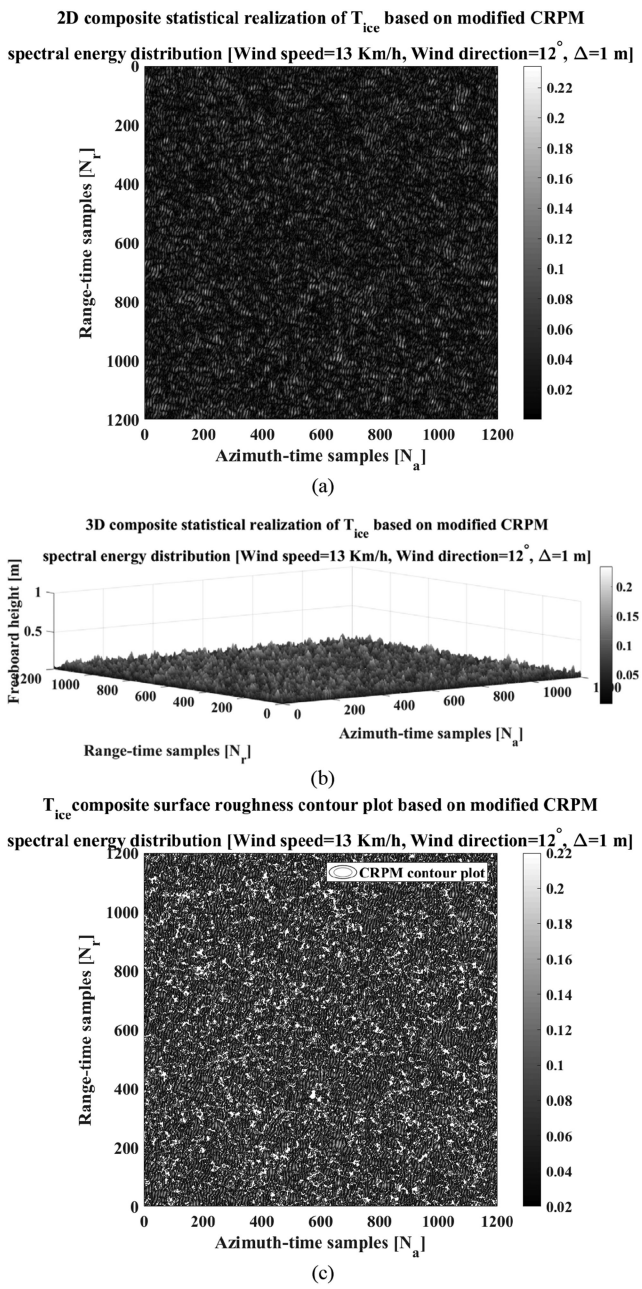

Fig. 4. CRPM roughness under the reference sea state conditions of wind speed = 13 km/h, $\theta = 12^{\circ}$, and $\Delta = 1$ m. (a) 2-D. (b) 3-D. (c) Contour plot.

fluctuations are significantly affected by a predictable pattern of sea state [78]. However, the fact that the freeboard changes relative to the sea state indicates its direct contribution to the redistribution of $\boldsymbol{T}_{\mathrm{ice}}$ energy components. In other words, energy couplings that can dampen waves, the boundary setting that modifies the energy convergence, and the intermodulation effects that directly affect the scatterings play roles in the balance of (13) and the transformation of $\boldsymbol{T}_{\mathrm{ice}}$ [80]. As an approach, extracting the determinative spectral properties of CRPM under the sea state would help in investigating the behaviors of composite components and their wave interactions.

To this end, PSD properties of $D(\omega, \theta)$ based on gamma PDF in conjunction with a wind speed of 13 km/h and direction of

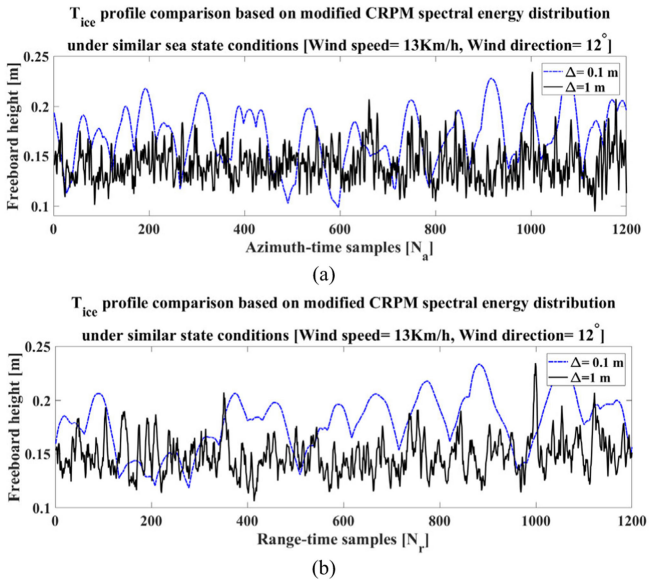

Fig. 5. CRPM freeboard height profile estimation with fixed wind speed 13 km/h, fixed wind direction $\theta = 12^{\circ}$ and variable resolutions $\Delta = 0.1$ m and $\Delta = 1$ m. (a) Azimuth direction. (b) Range direction.

12° as well as 0.1 m resolution, hereinafter referred to as the reference sea state condition, have been estimated in both range and azimuth directions, as shown in Fig. 8. As seen, a low-frequency peak of 1 dB can be found in both directions while they have slight differences in their spatial distribution of medium and higher scales of frequency components. This is due to the formulation of the CRPM based on (10) and the sensitivity of higher frequency scales to the spectral distribution as a function of sea state. In other words, the PSD of $D(\omega, \theta)$ is associated with the scattering components of short and medium scales of ocean modulations in (18). It is worth noting that the PSD profile is simulated based solely on the directional distribution of $D(\omega, \theta)$, whereas the effects of $N(\omega)$ in the form of optimization function are neglected here due to further detailed investigation in the following sections.

Similarly, the PSD profile of $D(\omega, \theta)$ for the reference CRPM function under different sea state conditions was modeled and compared with the conditions in Figs. 9 and 10. As seen in Fig. 9(a) and (b), the maximum magnitude of the PSD difference profile in the case of the speed alteration scenario is approximately 0.1 dB, which is much stronger than its direction deviation counterpart, with a value of 0.03 dB in Fig. 10(a) and (b). It can also be deduced that the order of changes in both directions has no specific pattern and mostly follows the same random attributes of Figs. 6 and 7. Regardless of the maximum values and their attributes in the direction deviation scenario in Fig. 10, the PSD difference profiles are generally limited to a few hundredth of dB, whereas the speed alteration scenario in Fig. 9 has a relatively stronger impact on the PSD. As a result, the control of $D(\omega, \theta)$ and the ice transfer function are limited by the sea state, whereas the wind speed plays a significant role in its directional distribution rather than the wind direction.

As a rule of thumb, in the case of speed values lower than the reference, the chance of similar spectral behavior to the reference PSD is more likely to occur than the higher values.

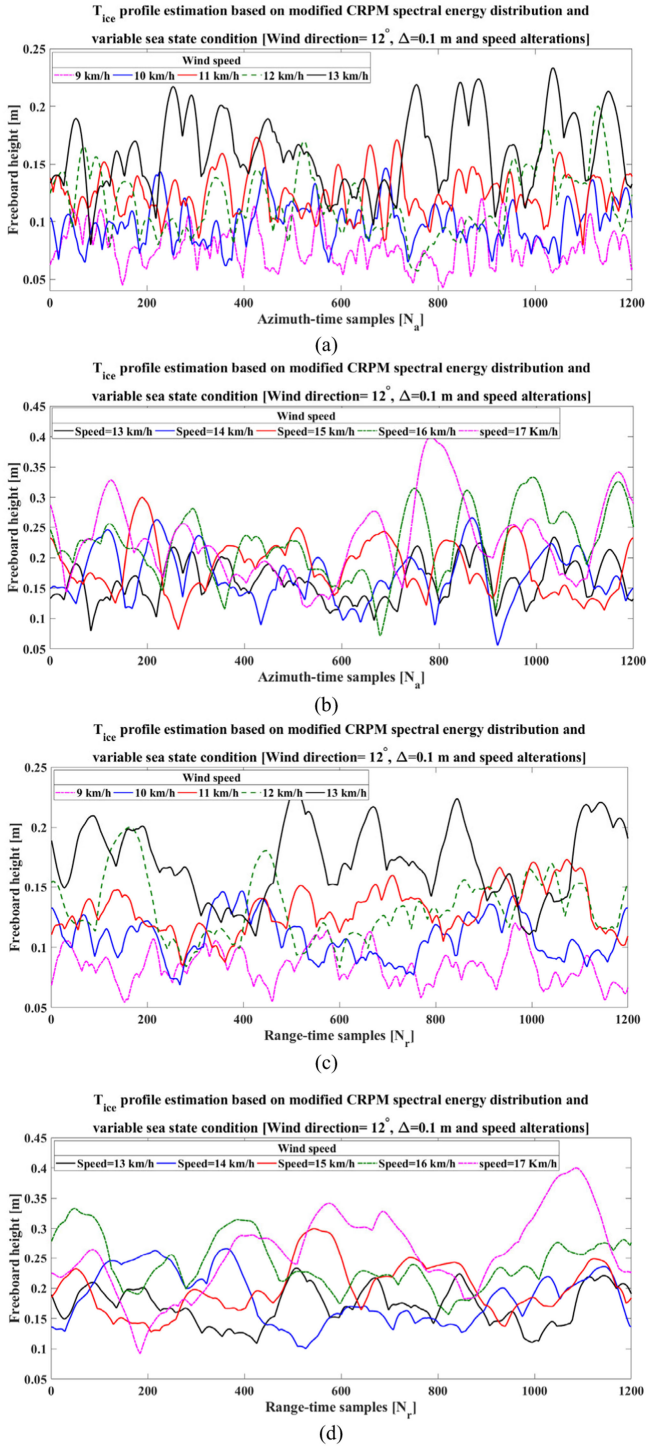

Fig. 6. CRPM freeboard height profile estimation with fixed wind direction $\theta = 12$ and variable speeds. (a) and (b) azimuth direction. (c) and (d) Range direction.

In other words, the higher the speed, the more significant the PSD difference would be. However, there is no such rule for the direction deviation scenario.

In short, CRPM surface roughness modeling in terms of ice transfer function computation is entirely dependent on PDF properties of the JONSWAP function, and their PSD levels are under the control of the sea state. However, there is no

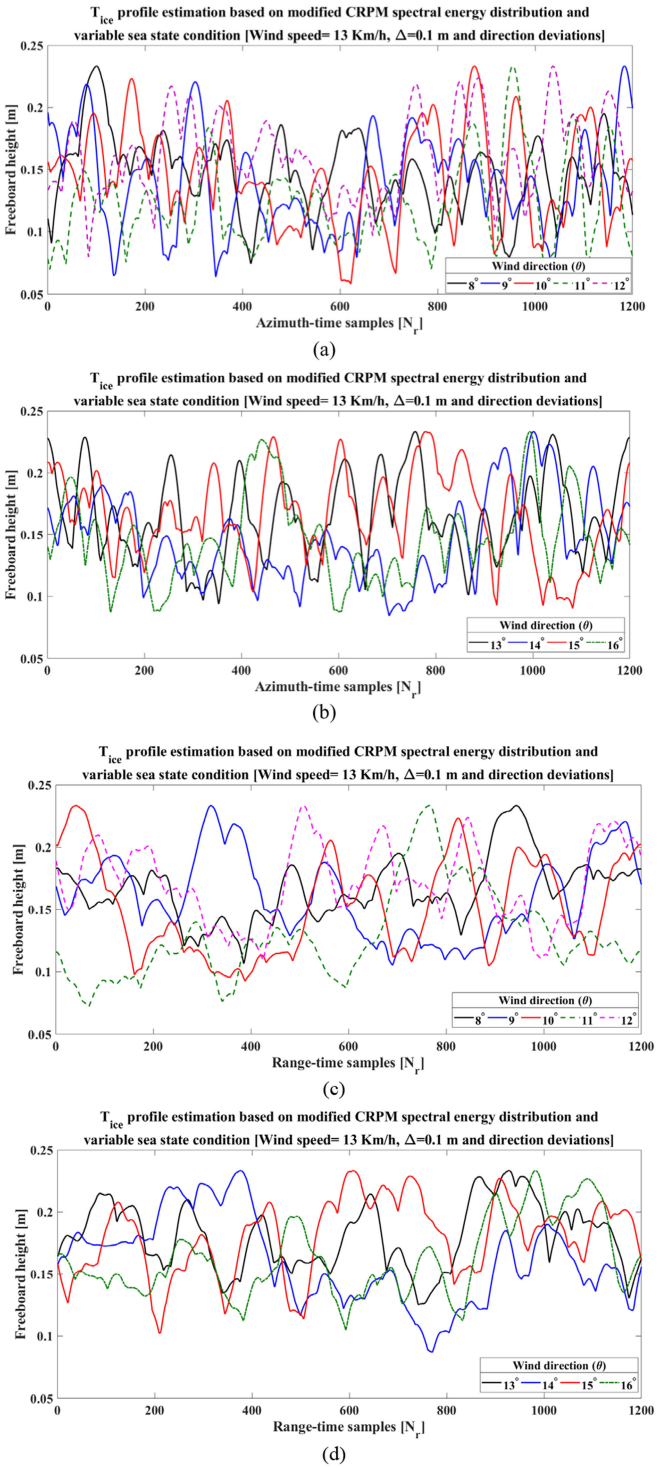

Fig. 7. CRPM freeboard height profile estimation with fixed wind speed 13 km/h and variable wind directions. (a) and (b) Azimuth direction. (c) and (d) Range direction.

specific pattern for the impacts of sea states on the surface roughness and its fluctuations. The result is shown in another way by surface mesh generation. To this end, after the roughness modeling procedure, it is converted into a triangular network based on a triangulation structure. This structure contains a set of vectors defining the vertices of the roughness and the continuous tetrahedral mesh that links them based on their different values.

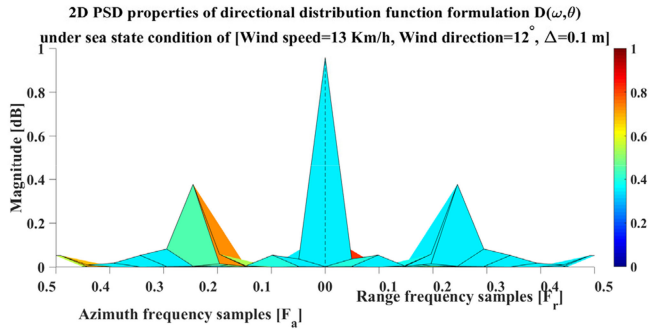

Fig. 8. 2-D PSD profile extraction of directional distribution function $D(\omega, \theta)$ under the reference sea state condition of wind speed $= 13$ km/h, $\theta = 12^{\circ}$, and $\Delta = 0.1$ m.

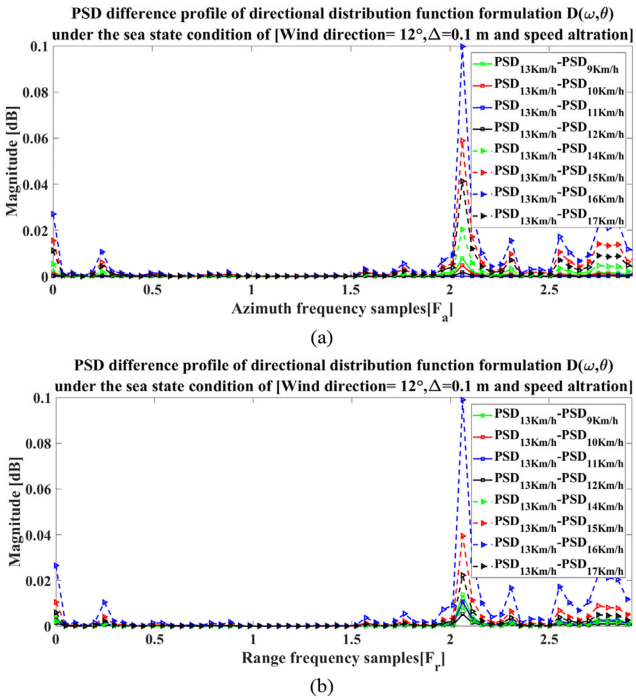

Fig. 9. PSD difference profile estimation of directional distribution function $D(\omega, \theta)$ under the reference sea state condition $\Delta = 0.1$ m with speed alterations. (a) Azimuth direction. (b) Range direction.

Fig. 11 presents the mesh structure of the surface under the minimum and maximum values of the sea state. Small and large sizes of tringles are linked together, which shows texture consistency, namely, surface roughness fluctuations. The small triangle concentrations present intense freeboard fluctuations or rapid alterations of roughness within the resolution cells, while the larger triangles are signs of homogenous texture behavior in a more harmonized way. The cluster of small triangles indicates high entropy regions within the CRPM known as highly textured areas, which have rapid roughness fluctuations. These highly textured areas suffer from high error rates due to their inherent spectral distribution. Hence, the energy redistribution under sea state conditions in terms of ocean wave modulations directly impacts the consistency of the texture and its roughness in the form of clusters of tringles that are linked together. In short,

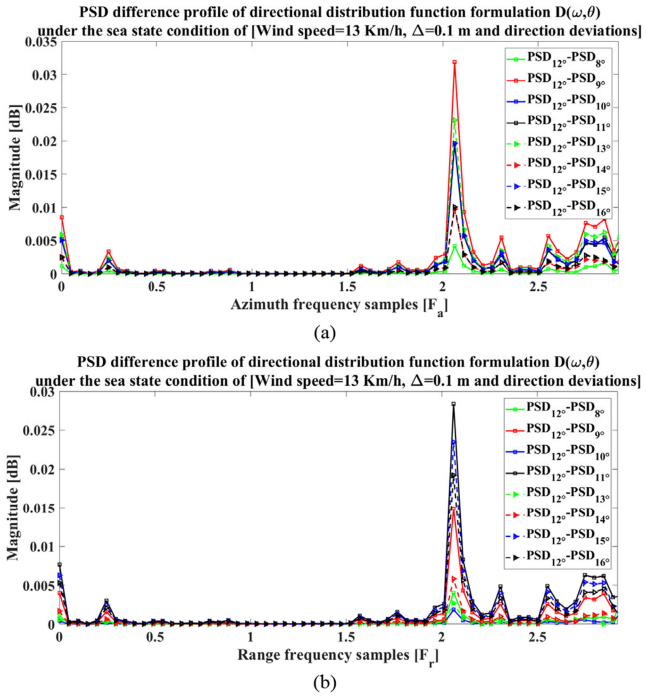

Fig. 10. PSD difference profile estimation of directional distribution function $D(\omega, \theta)$ under sea state condition $\Delta = 0.1$ m with direction deviations. (a) Azimuth direction. (b) Range direction.

these congested clusters of small triangles present unstable areas within the texture of the CRPM, which result from ocean wave modulation effects and their energy distribution. It is also noteworthy that the above-mentioned surface roughness, in the shape of triangular structures of the texture in collaboration with the JONSWAP spectrum, would result in different PSD behavior if the spectrum function or the sea state condition changes. As a result, the presence of roughness fluctuations is inevitable in the surface modeling, but the level of their presence depends on the sea state and its formulation.

III. CRPM Texture Statistical Distribution Formulation and Synthesis

The statistical interpretation of CRPM properties under a particular sea state condition is crucial for texture synthesis. However, due to the highly dynamic nature of CRPM under sea states, the presence of highly textured areas in the form of roughness fluctuations presents a challenge to such texture interpretation [49]–[51], [53], [57], [73]. On the other hand, these embedded fluctuations not only reduce the ability to resolve fine details but also make the evaluation of roughness modeling difficult. To overcome this inherent drawback, an amplitude or intensity evaluation of the presence of such roughness anomalies is important. Many evaluation techniques have been proposed, some relying on physical hypotheses of scattering mechanisms and others relying on more empirical formulation. On the one hand, the texture-based approach is assumed to be a proper alternative for such information investigation. On the other hand, due to the

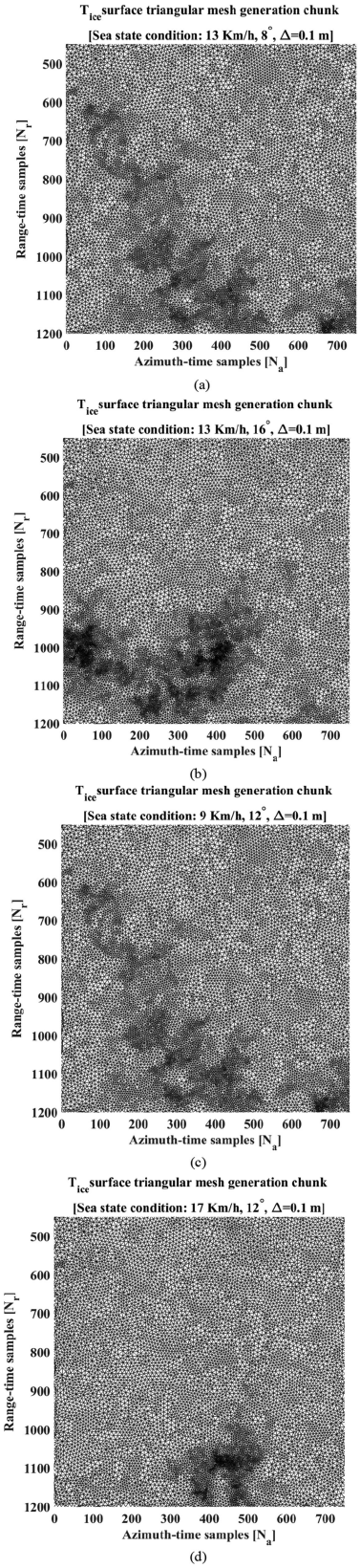

Fig. 11. CRPM surface triangular mesh generation chunk view with fixed resolution $\Delta = 0.1\ m$ and variable sea state conditions. (a) 13 km/h and $\theta = 8^\circ$. (b) 13 km/h and $\theta = 16^\circ$. (c) 9 km/h and $\theta = 12^\circ$. (d) 17 km/h and $\theta = 12^\circ$.

significant contribution of highly textured areas to the energy dissipation and spectrum redistribution of energy components, every evaluation scenario should be dependent on roughness fluctuations and their adverse effects, which have not yet been reported. To this end, spectral modeling of the highly textured areas and their electromagnetic interaction investigation along with their texture tension synthesis are considered the solutions to the evaluation of such inherent roughness anomalies. Hence, the focus of this section is on the highly dynamic CRPM texture and the assessment of intrinsic roughness fluctuations under the condition of a modified distribution function in (18).

A. CRPM Highly Textured Area Formulation and Simulation

As previously described, due to the dynamic spectral behavior of F_{CRPM} in the presence of ocean waves, independent scattering components within resolution cells will generate random roughness fluctuations in the form of highly textured areas. The characteristics of these multiplicative roughness anomalies differ from those found in other reference functions under different sea state conditions, such as their magnitude, PDF, energy distribution, and modulation effects. Hence, as the sea state changes, these inherent anomalies will be tuned based on the expectation and variance of samples. In short, a proper analysis of highly textured areas would help further evaluate the modeling procedure of CRPM and provide insight into the statistical distribution of scattering centers. According to Fig. 1, let us consider a 2-D roughness map of CRPM, after frame formatting provides the following model:

$$h = r_m \, . r_e \tag{26}$$

where h is the freeboard height, r_m is the roughness magnitude, and r_e is the intensity of inherent anomalies, which are two random independent variables within the resolution cell in a multiplicative manner [49]–[51], [53], [57], [73]. Accordingly, h_1 and h_2 can be described as two adjacent cells over the texture with the distance of resolution Δ as

$$\begin{aligned} h_1 &= \alpha r_e \\ h_2 &= \beta r_e \end{aligned} \tag{27}$$

where α and β are the roughness rates and r_e is an independent random fluctuation with identical PDFs that follow the modified gamma distribution $\Gamma(n, \lambda)$ in (18) as

$$p\ (r_e) = \frac{\lambda^n}{(n-1)!}\, {r_e}^{n-1} \exp\left(-\lambda r_e\right) \tag{28}$$

Hence, if $\alpha = \beta$, the two adjacent cells h_1 and h_2 belong to a homogenous texture. Otherwise, h_1 and h_2 are heterogeneous samples with different specifications. Accordingly, if $\alpha \neq 0$ and $\beta \neq 0$, h_1 and h_2 follow the general gamma PDF as

$$p_{h_1}\ (r_e) = \frac{\lambda^n}{\alpha\,(n-1)!}\ \left(\frac{r_e}{\alpha}\right)^{n-1} \times \exp\left(\frac{-\lambda}{\alpha} r_e\right) \text{ where } r_e, n \geq 0,$$

$$\text{and } p_{h_2}\ (r_e) = \frac{\lambda^n}{\beta\,(n-1)!}\ \left(\frac{r_e}{\beta}\right)^{n-1} \times \exp\left(\frac{-\lambda}{\beta} r_e\right) \text{ where } r_e, n \geq 0 \tag{29}$$

The properties of h_1-h_2 are the basis for highly textured area and roughness anomalies. Hence, if the cumulative distribution function of h_1-h_2 is defined as

$$P(h_1 - h_2 < t) = \iint_{r_e \leq t} p_{h_1}\left(r_e\right) p_{h_2}\left(r_e\right) dr_e \tag{30}$$

then the following will result:

$$P(h_1 - h_2 < t) = \begin{cases} \exp\left(-\frac{\lambda}{\beta}\left|t\right|\right) \frac{\lambda^n}{\alpha^n (n-1)!} \sum_{i=0}^{n-1} \frac{\lambda^i}{\beta^i} \\ \quad \left[\sum_{j=0}^{i} \frac{|t|^{i-j}}{j!(i-j)!} \frac{(n+j-1)!}{\left(\frac{\lambda}{\alpha}+\frac{\lambda}{\beta}\right)^{n+j}}\right] \quad t \leq 0 \\ 1 - \exp\left(-\frac{\lambda}{\beta}\left|t\right|\right) \frac{\lambda^n}{\alpha^n (n-1)!} \sum_{i=0}^{n-1} \frac{\lambda^i}{\beta^i} \\ \quad \left[\sum_{j=0}^{i} \frac{|t|^{i-j}}{j!(i-j)!} \frac{(n+j-1)!}{\left(\frac{\lambda}{\alpha}+\frac{\lambda}{\beta}\right)^{n+j}}\right] \quad t > 0 \end{cases} \tag{31}$$

As a result, the PDF of h_1-h_2 can be derived as

$$p_{h_1-h_2}\ (r_e) = \frac{\exp\left(-\frac{\lambda}{\beta}\left|r_e\right|\right)}{(n-1)!}\ \left(\frac{\lambda}{\alpha}\right)^n \left(\frac{\lambda}{\beta}\right)^n \times \left[\sum_{j=0}^{n-1} \frac{(n+j-1)!}{j!\,(n-j-1)!\left(\frac{\lambda}{\alpha}+\frac{\lambda}{\beta}\right)^{n+j}} |r_e|^{n-j-1}\right] \tag{32}$$

Hence, the instantaneous value of h_1-h_2 can be derived by

$$E\ \left[{r_e}^i\right] = \frac{2}{(n-1)!}\ \left(\frac{\lambda}{\alpha}\right)^n \left(\frac{\lambda}{\beta}\right)^n \times \left[\sum_{j=0}^{n-1} \frac{(n+j-1)!\,(i+n-j-1)!}{j!\,(n-j-1)!\left(\frac{\lambda}{\alpha}+\frac{\lambda}{\beta}\right)^{n+j}} \left|\frac{\beta}{\lambda}\right|^{i+n-j}\right] \text{ if } i \text{ is even}$$

$$E\ \left[{r_e}^i\right] = 0 \text{ if } i \text{ is odd.} \tag{33}$$

For the behavioral modeling of roughness fluctuations, let $\alpha = \beta = 1$. Then, (32) can be rewritten as

$$p_{h_1-h_2}\ (r_e) = \frac{\exp\left(-\lambda\left|r_e\right|\right)}{(n-1)!}\ (\lambda)^{2n} \times \left[\sum_{j=0}^{n-1} \frac{(n+j-1)!}{j!\,(n-j-1)!(2\lambda)^{n+j}} |r_e|^{n-j-1}\right] \tag{34}$$

Equation (34) is a combination of EP functions, and if a random roughness sample follows the EP function, it can be called EP(n, λ). Accordingly, the EP distribution and its corresponding statistical features are the basis of highly textured areas. Hence, an analysis of joint resolution cells Δ_i within a certain interval of frequencies based on their energy distribution in the form of PSD function modeling would help in investigating inherent roughness fluctuations of such a high entropy area within the CRPM surface. As a result, the PSD function of the texture in Fig. 3 and its inherent highly textured areas under the reference sea state are investigated and presented in Fig. 12.

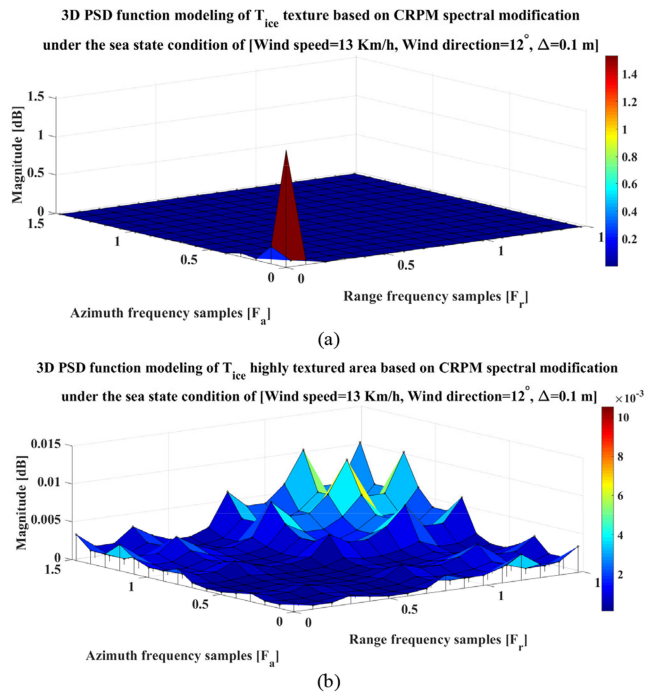

Fig. 12. 3-D PSD function profile estimation of T_{ice} texture information under the reference sea state condition of wind speed = 13 km/h, $\theta = 12^{\circ}$, and $\Delta = 0.1$ m. (a) Main body of texture information. (b) Highly textured area information.

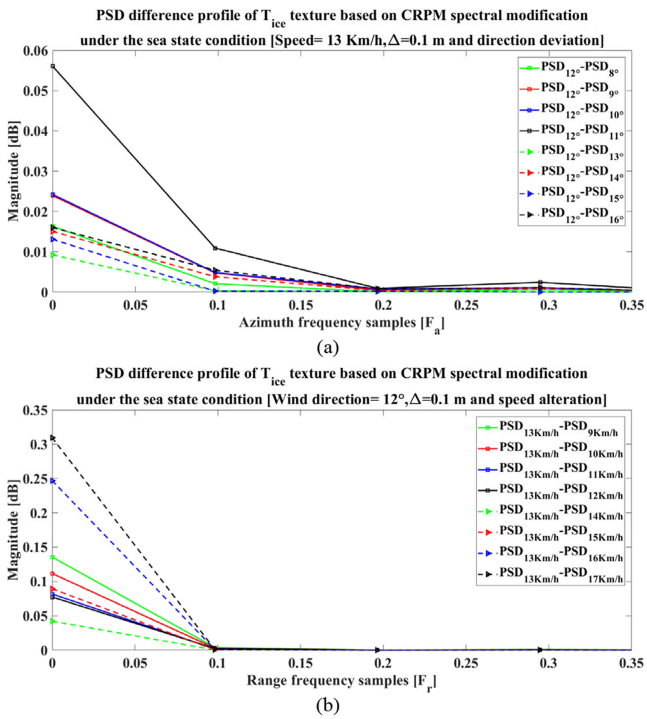

Fig. 13. PSD function difference profile estimation of T_{ice} low-frequency component texture information analysis under the reference sea state condition of $\Delta = 0.1$ m with (a) speed alterations and (b) direction deviation.

As seen in Fig. 12(a), the major peak in the low-frequency part on the corner of the spectrum represents the major spectral components of CRPM in the shape of nonoverlapping structures known as major entities or main bodies of texture. In comparison to the PSD function of $D(\omega, \theta)$ under the same sea state condition in Fig. 8, the PSD magnitude of the major entity in Fig. 12(a), which is the direct result of $D(\omega, \theta)N(\omega)$ and the application of ξ, not only amplifies by approximately 0.5 dB but also suppresses the high-frequency components $S_h(\omega)$ due to its modifications. It is worth noting that high-frequency components are maintained within the texture and are transformed into highly textured areas or overlapping structures, which exist in the form of several high-frequency peaks in the PSD function as in Fig. 12(b). As shown, highly textured areas with higher entropy or simply inherent roughness fluctuations mainly consist of medium and higher scales of scattering components, whereas their PSD magnitudes are approximately a hundredth of their low-frequency counterparts in Fig. 12(a).

In short, low-frequency components of the modified JONSWAP spectrum shape the major entity of the CRPM texture, whereas high-frequency components transform into highly textured components with higher entropy that are mostly sensitive to the sea state and are a potential source of roughness fluctuations. Hence, a complete PSD profile evaluation under different sea state conditions for both the low-frequency and high-frequency components would help understand the texture interactions and scattering behaviors of medium. Accordingly, the PSD profile of $S_l(\omega)$ in terms of the major entity and $S_h(\omega)$ in the form of a highly textured area are extracted under different sea states, as shown in Figs. 13 and 14.

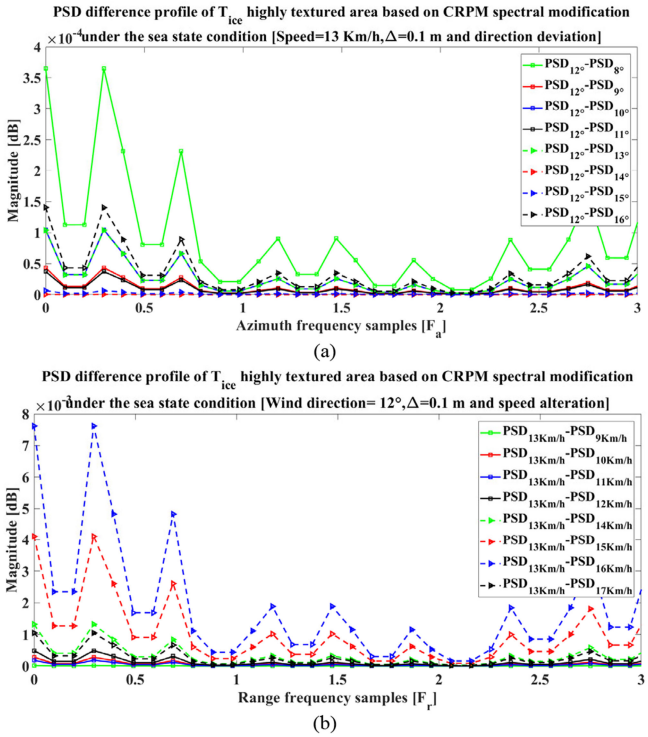

Fig. 14. PSD function difference profile estimation of the T_{ice} high-frequency component related to the highly textured area under the reference sea state condition of $\Delta = 0.1$ m with (a) speed alterations and (b) direction deviation.

The results present spectral interactions and texture characteristics in the form of two-scale frequency component under different sea states while being compared with the reference condition. As seen, both the wind speed alteration and direction deviation directly impact the PSD while there is no specific pattern for their changes or attenuations. As shown in Fig. 13(a), the spectral response of low-frequency components to the speed alteration is relatively stronger than the wind direction deviation in Fig. 13(b). According to Fig. 13(a), the maximum attenuation is approximately 0.33 dB for a speed difference of 1 km/h, from 13 km/h to 12 km/h, whereas the maximum attenuation for wind direction deviation is derived to be approximately 0.06 dB for a total of 4° of difference from 8° to 12°. In short, the low-frequency components in the form of the major entity within the texture of the CRPM are mostly under the control of wind speed with stronger magnitudes rather than the wind direction. However, speed has a limited range of frequency interactions compared to the direction. As shown in Fig. 13, the valid domain of frequency interactions to the wind direction in the case of the low-frequency component is almost three times larger than the speed alteration. In other words, wind direction affects the low-frequency components of JONSWAP in a wider spectral range but with smaller magnitudes rather than speed.

Similarly, PSD profile extraction for the highly textured area or the high-frequency component is presented in Fig. 14. As shown in Fig. 14, the high-frequency components are more responsive to ocean scatterings in a broader range of spectrum than their low-frequency counterparts in Fig. 13. However, the magnitude of speed alteration in Fig. 14(a) is relatively smaller than that in Fig. 13(a). Similar to Fig. 13(a), the speed alteration in Fig. 14(a) plays an important role in the spectral distribution compared to its wind direction deviation counterpart in Fig. 14(b), which is approximately ten times stronger. It is worth noting that in comparison to Fig. 13, high-frequency components in the form of roughness fluctuations are responsive to sea states over a wide range of frequencies due to their spectral interactions. In other words, the high-frequency components of CRPM spectrum are responsive to ocean scatterings over a wide range of frequencies, or simply, the roughness fluctuations are wideband modulation effects of the sea state conditions. However, due to macroscale specifications of JONSWAP formulation based on the swell regime, microscale features of ice such as ice dimensionality and their scattering effects are not included in the high-frequency components. Accordingly, the low-frequency components $S_l(\omega)$ act as a low-pass filter for ocean scatterings and its modulation effects, whereas the high-frequency components $S_h(\omega)$ inherently contain wideband modulation effects of ocean scatterings. Therefore, the roughness model of CRPM is derived from its two-scale scattering function, which makes the fluctuations to be dependent on modulation effects. As a result, the modified scattering function of CRPM has direct impact on roughness and texture characteristics.

Since the sensor cannot extract the sea state conditions, and because of inherent limitations for the reconstruction of 2-D image, the texture analysis is not fully reliable based on pixel information. Accordingly, any investigation on the visualized texture would help predict the backscattering properties of fractal roughness, and their pertinent fluctuations under the sea state conditions. Hence, the electromagnetic interaction analysis of CRPM and its backscattering modeling would help to further understand the composite nature of CRPM.

B. CRPM Texture Electromagnetic Interaction Evaluation

The result of the surface modeling of CRPM based on the modified JONSWAP energy function is a numerical matrix $\boldsymbol{T}_{\mathrm{ice}}$ that presents roughness in terms of complex values. The contribution of these values to surface electromagnetic interactions is important for texture homogeneity evaluation and energy coupling capabilities. Therefore, the RDG and spatial profile extraction of CRPM under different sea state conditions in the sense of SAR along with their objective metric assessments are considered here. The prerequisite for such evaluation is the development of a roughness matrix that meets the grayscale criterion of SAR imagery. To this end, complex values are assumed to be pixel intensities, whereas the original aspect ratio during the transformation procedure is maintained. Accordingly, each sample of the matrix is interpreted as the corresponding SAR image pixel based on its grayscale range span. The major steps of such transformation are grayscale normalization and the stretching of values within the scale. In addition, specific classes are applied to identify the lower and upper limits of the array that make the roughness matrix a complex homogenous terrain.

The result of the roughness transformation into the SAR grayscale image is presented in Fig. 15(a). As discussed previously, due to the high dynamics of CRPM under sea state conditions, the presence of a highly textured area is inevitable. Hence, the transformed image would be responsive to these inherent fluctuations in terms of pixel anomalies. Fig. 15(b) presents an advection map of the presence of inherent roughness fluctuations, hereby referred to as pixel anomalies. From an SAR point of view, these pixel anomalies result from the uncorrelated and noncoherent backscattering of the nondeterministic and completely time-dependent structure of surface, which can easily affect the reflection in the shape of dephased echo with diverse backscattering coefficients. The result in Fig. 15(c) presents a kurtosis map of embedded pixel anomalies related to Fig. 15(a), which is derived based on their probability distribution among the adjacent cells. As seen in Fig. 15(b) and (c), specific areas are distinguished from other homogenous textures due to the tailedness of their distribution, which not only gives them large gradient values but also makes them responsive to the sea state in the form of anomalies. As a result, random roughness fluctuations are most likely to occur in these areas, which are called unstable regions.

Therefore, along with CRPM roughness evaluation in Sections II and III-A, spatial resolution investigation based on the RDG might help better understand the electromagnetic interactions of surface. It should be noted that, in comparison to the abovementioned evaluations, spatial resolution profile is not only dependent on the surface roughness but also relies on SAR sensor parameters, such as the carrier frequency and the observation time. However, the results of electromagnetic interaction analysis are not parameter oriented, which implies that sensor parameters will not change the properties of CRPM.

The spatial resolution analysis is an active evaluation of sensor-terrain interactions in the form of phase history. In this

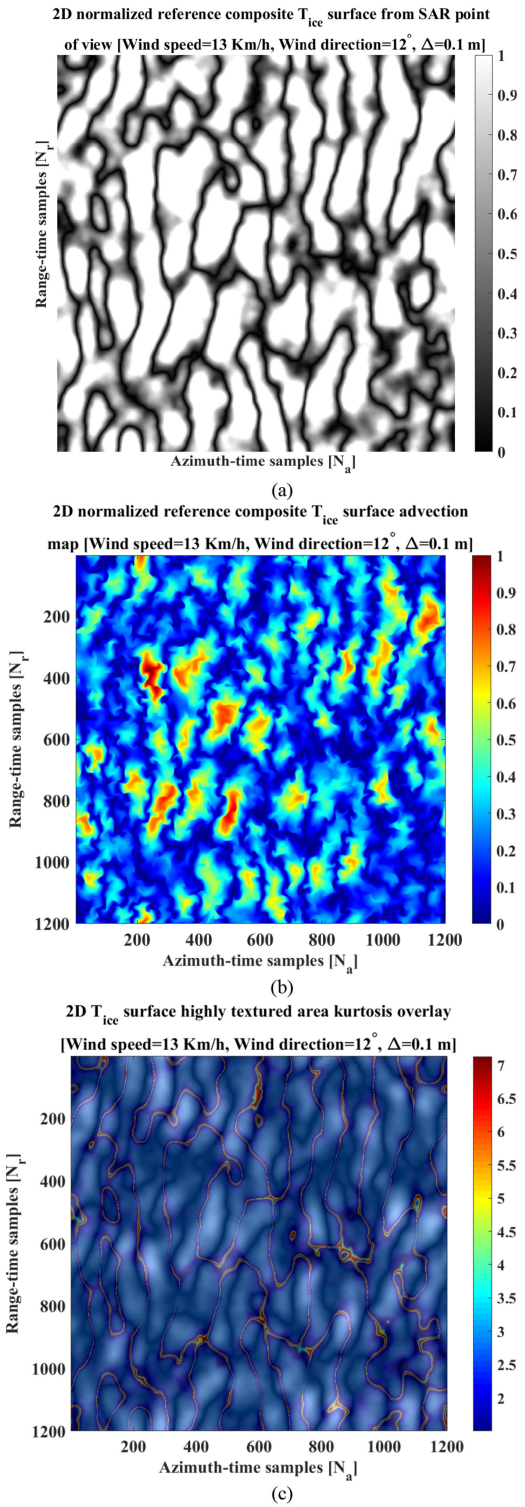

Fig. 15. T_{ice} Surface texture presentation based on (a) SAR point of view, (b) advection map analysis, and (c) highly textured area kurtosis image overlay.

research study, the RDG is carried out on the basis of a hybrid-domain processing algorithm based on Table I and the routines in Fig. 16 [72]. It is worth noting that the selection of parameters for RDG is dependent on the size of the texture. Referring to the proposed RDG method in Fig. 16, incoherent information of the reference transformed grayscale image of CRPM will

TABLE I
SYSTEM PARAMETERS OF THE SENSOR FOR SPATIAL PROFILE

Parameter	Value
Carrier frequency	9.2 GHz
Repetition frequency	4 KHz
Maximum duty cycle	0.2
Pulse width	0.4 μsec
3dB Bandwidth	60 MHz
Scaling factor	1

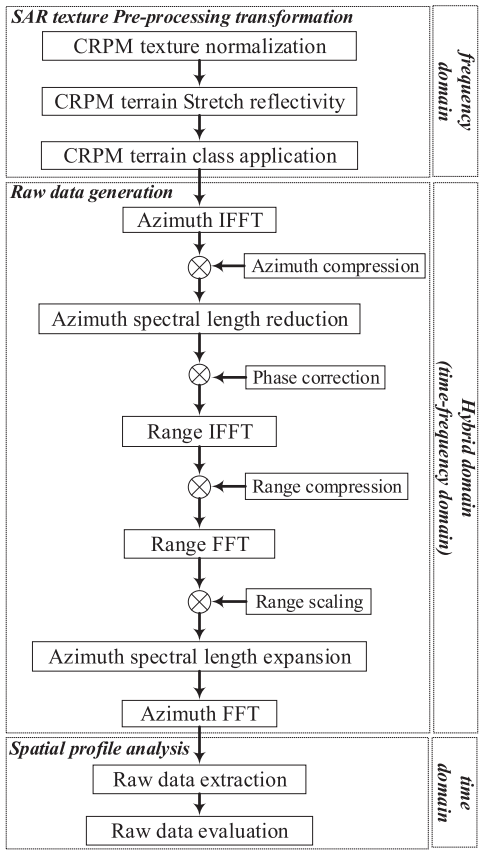

Fig. 16. CRPM raw data generation procedure based on the hybrid-domain SAR algorithm.

be imported to the algorithm first. As a result, the received backscattered data from the surface of CRPM are simulated and presented in Fig. 17(a), whereas its heat map is overlaid on the reference image in Fig. 17(b). As can be seen, the homogenous ice floes have stronger reflectivity and better uniformity in the texture. As the texture changes to open water, including the edges, the magnitude attenuates, and its minimum value is derived to be approximately 0.46 dB. All these reflectivity variations generate noncoherent phase modulations that will be transform into highly textured areas over the entire surface known as roughness fluctuations. The kurtosis result in Fig. 17(c) presents these anomalies in the form of uncorrelated variations and noncoherent reflectivity within the phase history. As seen, these uncorrelated backscattering and roughness fluctuations are mainly found in the open water and their edges. The peak values in Fig. 17(c) indicate the severity of such noncoherency, which are signs of unstable regions as the major source of roughness

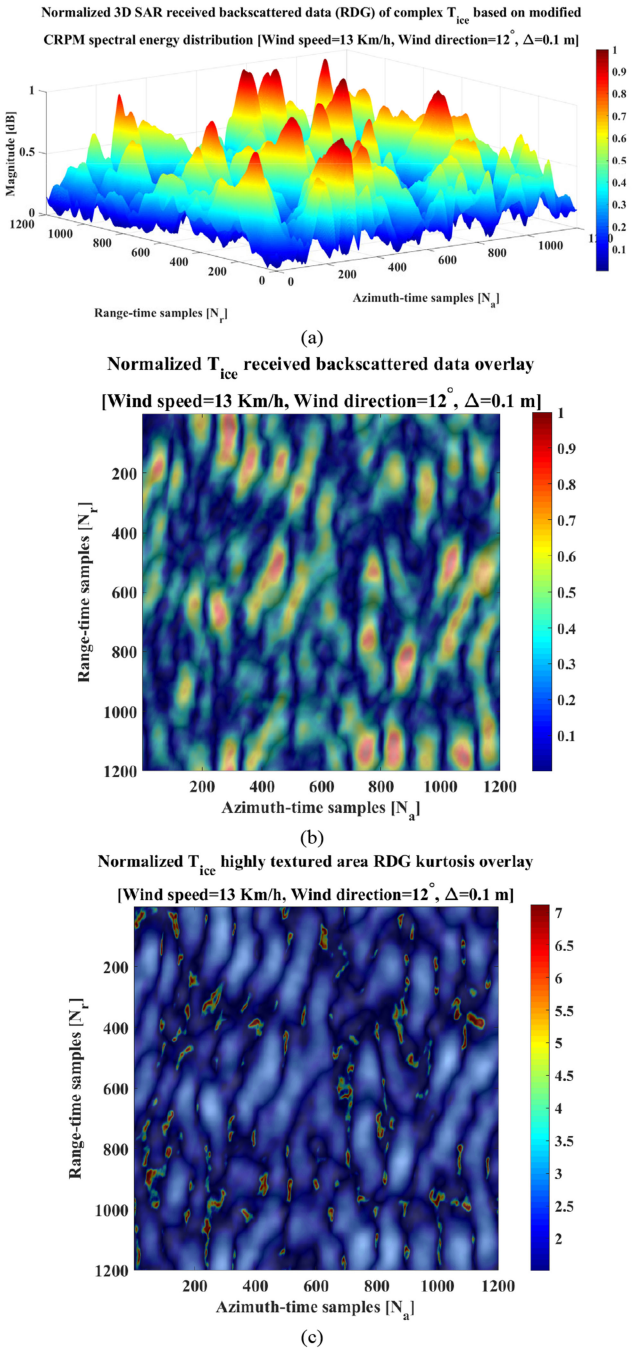

Fig. 17. Normalized SAR complex CRPM. (a) Received backscattered data. (b) RDG overlay with the reference image. (c) RDG kurtosis overlay with the reference image.

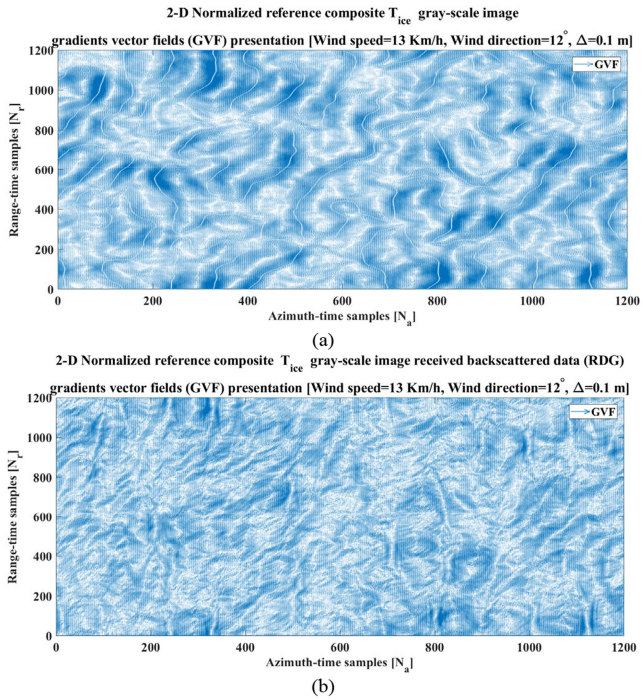

Fig. 18. Gradient vector field (GVF) presentation of (a) normalized reference SAR $T_{\rm ice}$ RDG and (b) normalized reference SAR $T_{\rm ice}$ image.

fluctuations and pertinent SAR texture anomalies. The higher the kurtosis, the more resolution cells will have the dominant attenuation; however, a uniform distribution of kurtosis is an extreme case that will not occur in a model, specifically while dealing with dynamic mediums such as CRPM.

As a result, between high-frequency components, i.e., $S_h(\omega)$, and noncoherent phase modulations, a contribution to the generation of roughness fluctuations can be found. As seen, the sensitivity of high-frequency components to the sea states will lead to intermodulation effects in the form of wideband ocean modulations that can generate uncorrelated reflections and subsequently signal noncoherency within the phase history, which are the source of SAR geometric distortions. The results in Fig. 18 present the presence of such texture anomalies in terms of a GVF map from the RDG and image points of view.

As seen, these noncoherent effects can generate a dense spatial cluster of GVFs within their resolution cells while being diffused to the neighboring cells in the form of uncorrelated anomalies. Therefore, RDG will be affected in both azimuth and range directions by the adverse presence of random surface fluctuations, as shown in Fig. 19. It should be noted that the RDG profiles are extracted based on two different scenarios, including the proposed method in Fig. 16 and the improved version with relatively suppressed fluctuations, known as damped version [70]. However, the enhanced version of RDG is an optimized case with a relatively minor loss of information that has pros and cons, but it is necessary to show how roughness fluctuations degrade the electromagnetic interactions. As shown in Fig. 19(a) and (b), the deteriorative effects of such anomalies on the spatial resolution tend to have a faster rate in azimuth direction rather than the range, whereas they have the same maximum instantaneous attenuation value of 0.1 dB per resolution cell and approximately 1.5 dB peak to peak. As shown in Fig. 19(c), the adverse presence of random roughness fluctuations directly contributes to the instantaneous attenuation of spatial resolution and SAR geometric loss. In other words, the resulting information loss is due to modulations effects in terms of two-scale frequency components. However, the azimuth direction in the spatial resolution profile is more sensitive to such loss due to its Doppler dependence, which is under the control of the boundary condition. Hence, inherent roughness fluctuations within the

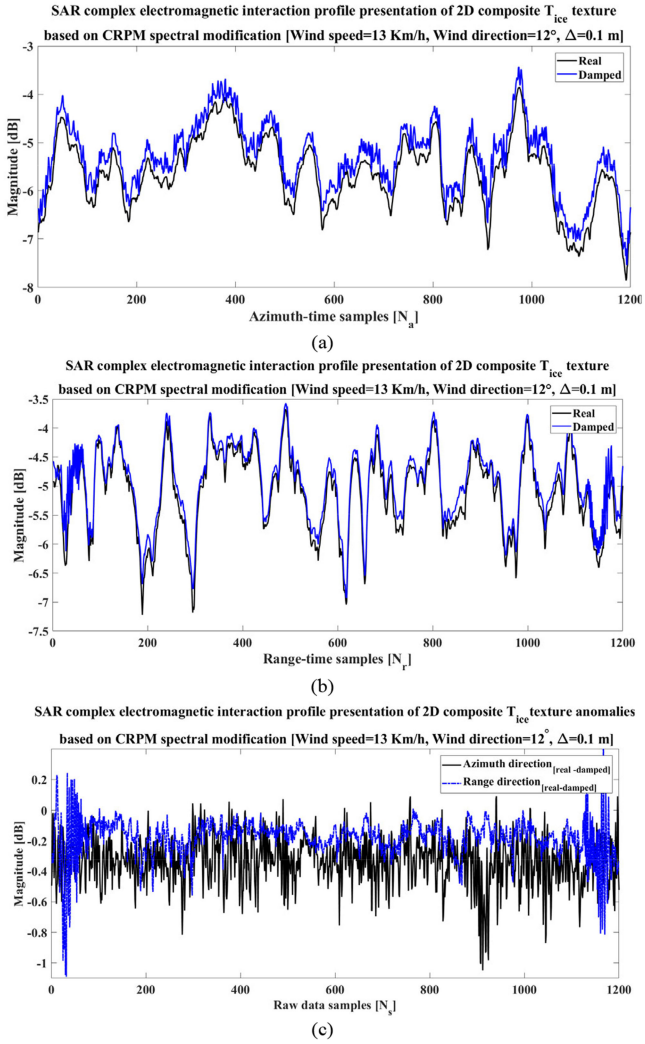

Fig. 19. SAR complex RDG profile presentation of $T_{\rm ice}$ surface texture under real and damped conditions. (a) Azimuth direction. (b) Range direction. (c) RDG difference profile in both directions.

texture are observed to be a normal destructive phenomenon with different rates and magnitudes based on sea states.

Since the information capacity per resolution cell is limited, the perfect suppression of these roughness anomalies is impossible without sacrificing the information. Thus, extracting the complete spatial resolution profile of CRPM as a function of sea state would be helpful for further roughness investigations and the pertinent evaluation of information loss. Hence, the normalized SAR received backscattered data of CRPM under sea state conditions in Figs. 6 and 7 with a wind speed of 13 km/h, wind direction of 12°, and resolution of 0.1 m within an area of 120 m × 120 m were generated and are presented in Fig. 20. As shown in Fig. 20, every specific texture has electromagnetic interactions, which bolsters the role of the sea state in terms of surface roughness modeling and electromagnetic interactions. As seen, every specific sea state, whether it is the speed alteration or the direction deviation, has its information loss and attenuation on the RDG. The peak-to-peak value of loss reaches approximately 1.5 dB, the same as the results in

TABLE II
RDG OBJECTIVE METRICS OF THE NORMALIZED CRPM SURFACE UNDER SEA STATE CONDITIONS [WIND DIRECTION $=12°$, $\Delta = 0.1$ m, AND SPEED ALTERATION]

Wind speed [km/h]	9	10	11	12	13	14	15	16	17
ISLR [dB]	-16.8	-5.0	-12.6	-13.7	-6.1	-6.5	-4.6	-16.0	-5.0
PSLR [dB]	-6.1	-8.0	-13.7	-4.5	-12.9	-15.5	-14.3	-16.2	-15.0

TABLE III
RDG OBJECTIVE METRICS OF THE NORMALIZED CRPM SURFACE UNDER SEA STATE CONDITIONS [SPEED $= 13$ KM/H, $\Delta = 0.1$ m, AND DIRECTION DEVIATION]

Wind direction [degree]	8	9	10	11	12	13	14	15	16
ISLR [dB]	-5.1	-5.08	-8.1	-9.3	-6.1	-16.5	-8.9	-6.4	-8.9
PSLR [dB]	-14.1	-11.6	-12.3	-12.4	-12.9	-10.9	-13.3	-9.8	-11.6

Fig. 19(c), whereas in the case of the spectral PDF, the sea state behaves differently, and the wind speed plays a critical role in the roughness fluctuations.

The peak-to-peak value of loss reaches approximately 1.5 dB, the same as the results in Fig. 19(c), while in the case of the PDF, the sea state behaves differently, and the wind speed plays a critical role in the formation of fluctuations. Hence, the way the sea state affects the roughness is different from the way it affects the electromagnetic interactions. In other words, sea state conditions have major impacts on the spectral components of JONSWAP and their PSD regarding the PDF modifications, while in the case of the electromagnetic interactions, they have similar attenuation profiles. As a result, the texture of CRPM is a nondeterministic structure that is constantly changing based on origination, formation, growth and melting as a function of sea state, while the electromagnetic properties follow a specific pattern of attenuation.

Accordingly, an objective quality assessment based on texture and its contribution to the electromagnetic interaction might help better understand the concept. The results in Tables II and III present SAR objective metrics based on peak side-lobe ratio (PSLR) and integrated side-lobe ratio (ISLR) estimation as a function of sea state conditions. The proposed evaluation method determines the ability of the sensor to identify random roughness fluctuations in the shape of noncoherent and uncorrelated backscattering from nearby strong reflectivities. Accordingly, the lowest ISLR and PSLR values are signs of better spatial resolution performance.

As listed in Tables II and III, in the case of speed alteration, the highest ISLR value is achieved at 15 km/h with a value of -4.6 dB, whereas the lowest ISLR is observed at 9 km/h with a value of –16.8 dB. Similarly, in PSLR measurements, the highest value is derived to be approximately -6.1 dB at 9 km/h, and the lowest value is derived to be -16.2 dB at 16 km/h. Furthermore, in the case of wind direction deviations, the highest value of ISLR is -5.1 dB at 8°, whereas the lowest value of ISLR is observed at 13° with -16.5 dB. Additionally, in the case of the PSLR measurement under the wind deviation scenario, the highest value is derived as -9.8 dB at 15°, and the lowest value is -14.1 dB at 8°. In short, the metrics in

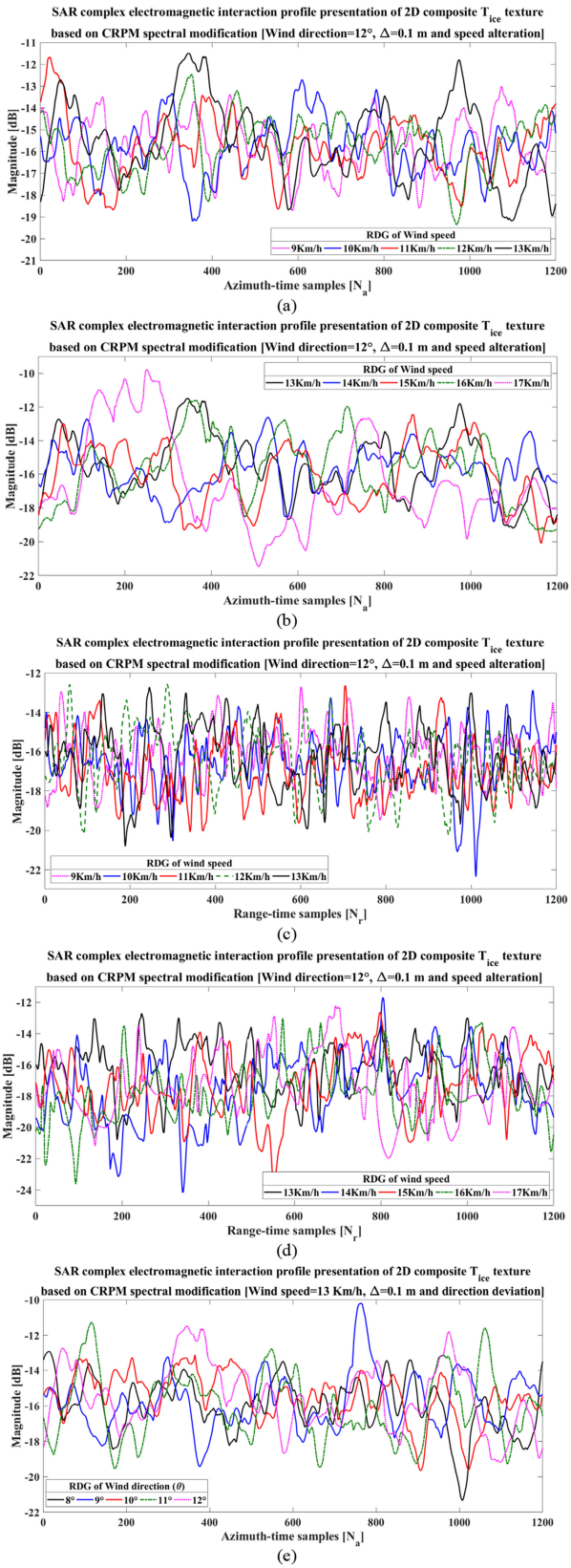

Fig. 20. SAR complex RDG profile presentation of T_{ice} surface texture under the reference sea state condition of $\Delta = 0.1$ m with variable speeds and directions. (a) and (b) Speed alteration—azimuth. (c) and (d) Speed alteration—range. (e) and (f) Direction deviation—azimuth. (g) and (h) Direction deviation—range.

Fig. 20. Continued.

Tables II and III confirm the whole roughness modeling procedure and simulation results, where the sea state affected the surface fluctuations and its electromagnetic interactions in a way different from the scattering components. The metrics also show that no specific sea state condition consistently outperforms the other when dealing with roughness and electromagnetic interactions. However, the evaluation of inherent roughness anomalies needs a complementary framework of synthesis. Therefore, a method of texture synthesis based on surface tension analysis in the aftermath of random roughness fluctuations would help rationalize the relationship between the metrics and simulations results. Hence, the next section will discuss the CRPM roughness tension synthesis based on the joint geometrical distribution of cells on a single scale of the texture.

C. CRPM Texture Tension Synthesis

From the SAR point of view, the texture of CRPM can be defined in terms of variations in the gray levels that describe the distribution of ice floes and open water based on a specific

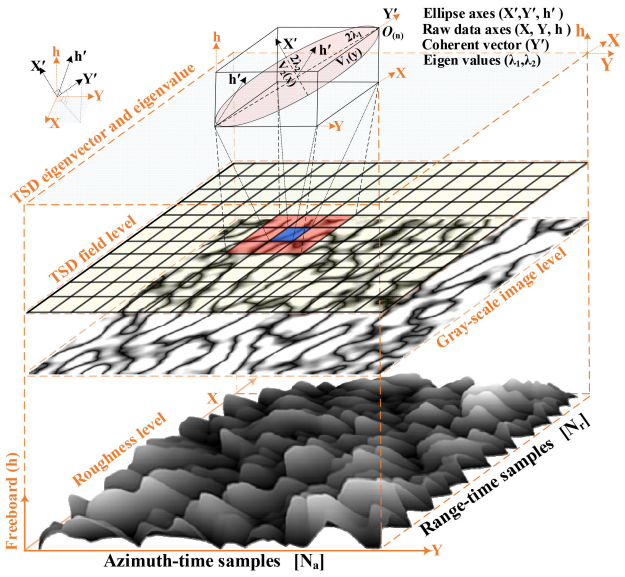

Fig. 21. CRPM surface roughness tension analysis based on TDS field map.

pattern as a function of sea state. Prior to this approach, however, the phase history of raw data was modulated by the surface characteristics in the shape of additional uncertainty within the spatial resolution profile. These nondeterminative and stochastic scattering phenomena will lead to noncoherent phase reception and reflectivity anomalies, which can result in the information loss. To date, several parametric and nonparametric algorithms have been proposed for the synthesis of texture anomalies and their pertinent geometrical loss [67], [73]. Unfortunately, most of these algorithms fail to extract the geometrical information of inherent structures with directional variations identical to the embedded roughness fluctuations. Since backscattering is highly sensitive to these geometrical anomalies and the reconstructed SAR image suffers from the relevant phase disorders, a surface tension synthesis based on geometrical information would be another novel approach to evaluate CRPM surface fluctuations [53]. In such an analysis, TSD field investigation, as a nonparametric method, has led to impressive results when dealing with anomalies [73]. As an approach, this patch-based method allows us to represent the tension of texture through the tensor analysis of roughness, taking into account both the local orientation energy and degree of anisotropy. As a result, the TSD field will summarize the predominant geometrical directions of the roughness gradient in a specified neighborhood of resolution cells and the degree to which those directions are coherent. Therefore, the proposed TSD synthesis is a numerical matrix that visualizes partial derivatives of geometrical information and their distribution pattern within the texture. Fig. 21 presents an overview of the TSD field visualization scenario for the purpose of CRPM roughness tension synthesis.

According to Fig. 21, the TSD field map, $\boldsymbol{S}_{\mathrm{CRPM}}$, of the texture, i.e., $\boldsymbol{T}_{\mathrm{ice}}$, is defined as the field of local covariance matrices of its partial derivatives in both the range and azimuth directions that have been derived from estimated gradients of texture, $\nabla \boldsymbol{T}_{\mathrm{ice}} = [\boldsymbol{T}_x \ \boldsymbol{T}_y]$, with $\boldsymbol{T}_x = \boldsymbol{T}_{\mathrm{ice}} * G_x$ and $\boldsymbol{T}_y = \boldsymbol{T}_{\mathrm{ice}} * G_y$, where G_x and G_y are Gaussian derivative kernels and $*$ denotes the convolution. Then, $\boldsymbol{S}_{\mathrm{CRPM}}$ is computed by spatial smoothing of the gradient output product of texture as

$$\boldsymbol{S}_{\mathrm{CRPM}} = G_\sigma * \nabla \boldsymbol{T}_{\mathrm{ice}} \nabla \boldsymbol{T}_{\mathrm{ice}}^T \tag{35}$$

where G_σ is a Gaussian averaging kernel with standard deviation σ and $\nabla \boldsymbol{T}_{\mathrm{ice}}^T$ is the transpose matrix of CRPM. Note that $\boldsymbol{S}_{\mathrm{CRPM}}$ is of the same size as the reference texture with $N_r \times N_a$, whereas $\boldsymbol{T}_{\mathrm{ice}}$ is applied in the form of its stretched version in Fig. 16. Spatial smoothing not only makes the TSD robust to roughness fluctuations but also harmonizes the random distribution of fluctuation orientations among the cells. The choice of σ is important to generate a relevant TSD map overlay; a high value of σ covers both the low- and high-frequency spectral components of CRPM in (10) and improves local orientation estimation. In contrast, a low value of σ ensures the major entity of local CRPM components, known as $s_l(\omega)$, has fewer geometrical disorders. It should be noted that the margin of σ is chosen according to the size of the texture to ensure that the Gaussian averaging window size is large enough to faithfully cover the fluctuations.

At each resolution cell position of n_i over the entire terrain, an eigenvalue decomposition of $\boldsymbol{S}_{\mathrm{CRPM}}(n_i)$ results in two nonnegative eigenvalues $\lambda_1(n_i)$ and $\lambda_2(n_i)$ that show the strength of the local roughness, i.e., the strength of the directional intensity fluctuations of the cell, and two corresponding eigenvectors $v_1(n_i) = [v_{1x}(n_i) \ v_{1y}(n_i)]$ and $v_2(n_i) = [v_{2x}(n_i) \ v_{2y}(n_i)]$ that point orthogonal and parallel to the local roughness of the resolution cell. The local orientation $O(n_i)$ in the direction of Y' is computed from the eigenvector $v_1(n_i)$ associated with $\lambda_1(n_i)$ that ranges between $-\pi/2$ and $\pi/2$ as

$$O(n_i) = \arctan\left(\frac{v_{1y}(n_i)}{v_{1x}(n_i)}\right) \tag{36}$$

The coherence factor is obtained from the TSD eigenvalues and ranges between 0 and 1, which can be considered a measure of the roughness local anisotropy as

$$C(n_i) = \frac{\lambda_1(n_i) - \lambda_2(n_i)}{\lambda_1(n_i) + \lambda_2(n_i)} \tag{37}$$

This approach also characterizes the geometrical dispersion of gradient orientation over the surface. In other words, the minimum value of C is equivalent to the most negative orientation, whereas the maximum value is equal to the maximum positive inclination of the ellipse within the coordinate system, which is a criterion for roughness fluctuations. Regarding the symmetric formulation of (35) and the application of Gaussian smoothing kernel, as well as calculating the corresponding eigenvalues, a bilinear mapping of eigenvectors in the form of a 2-D quadratic surface of ellipses with orientations of O and coherences of C will be overlaid on the texture of the CRPM. This tension computation procedure is repeated for the entire texture until the complete TSD field map is determined. To this end, a survey of TSD synthesis on the realized texture of CRPM and the pertinent received backscattered data was carried out and is presented in Figs. 22 and 23. As shown, the TSD field map focuses on the geometrical properties of resolution cells and their stochastic texture anomaly distributions.

According to the results in Fig. 22, the color of the TSD field map ranges from low to high coherency values of C, while

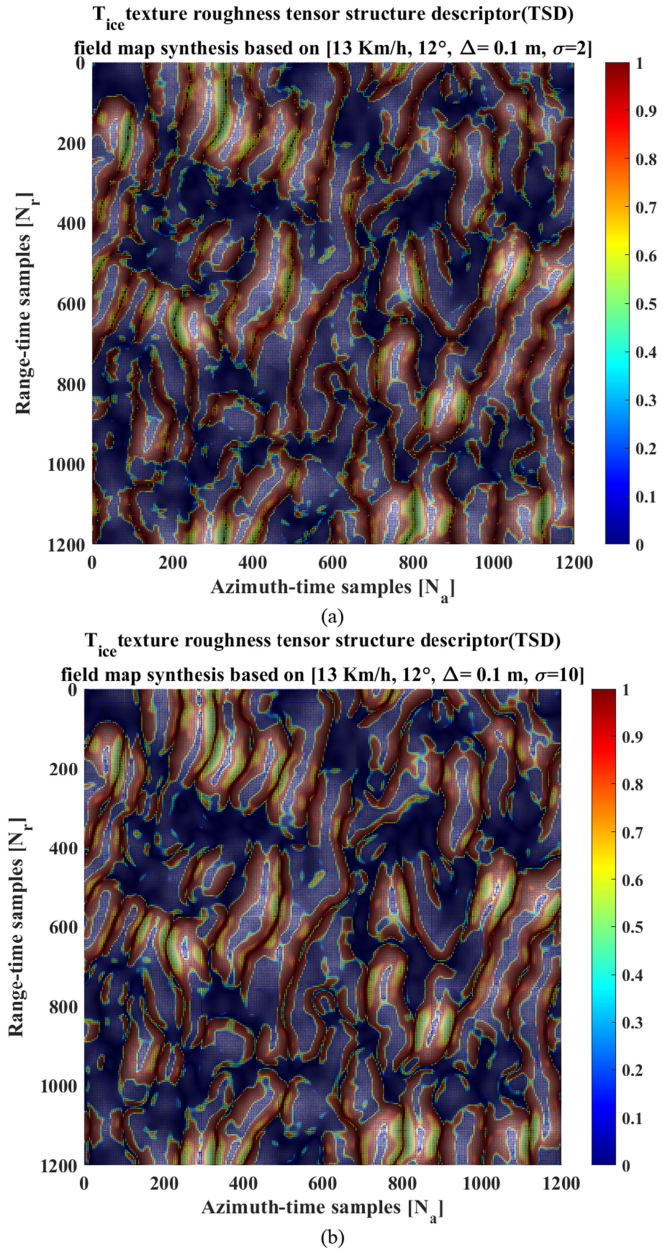

Fig. 22. CRPM surface roughness tension results based on TDS field synthesis of the reference sea state condition with wind speed = 13 km/h, $\theta = 12^{\circ}$, $\Delta = 0.1$ m, and pixel group of four. (a) $\sigma = 2$. (b) $\sigma = 10$.

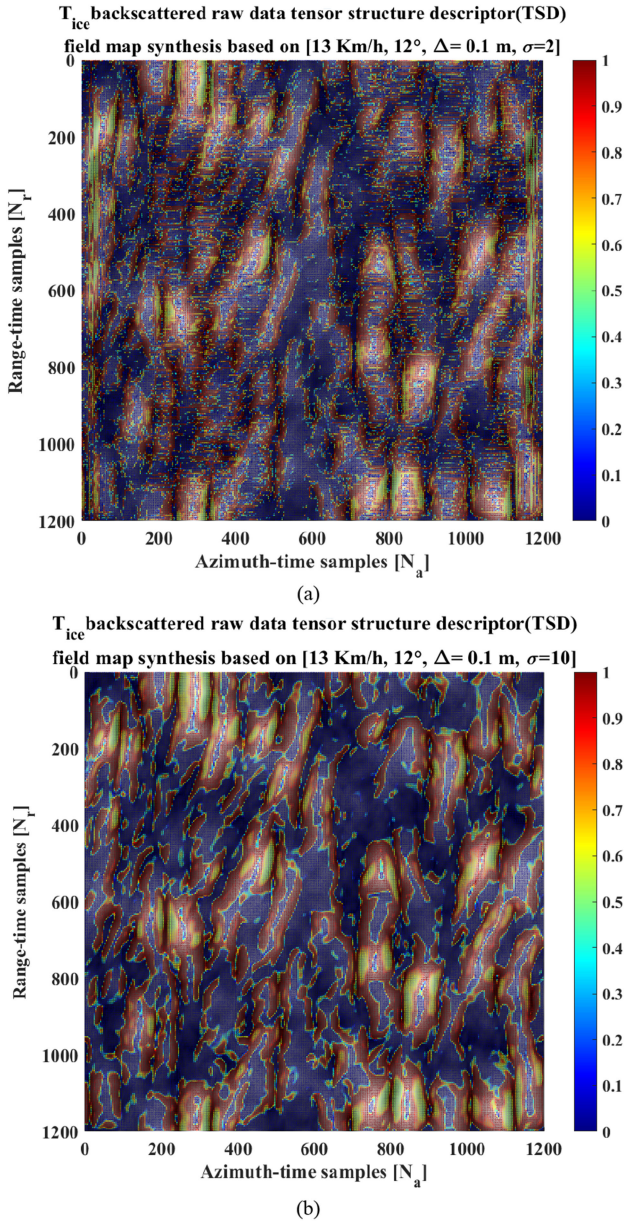

Fig. 23. CRPM received backscattered data tension results based on TDS field synthesis of the reference sea state condition with wind speed = 13 km/h, $\theta = 12^{\circ}$, $\Delta = 0.1$ m, and pixel group of four. (a) $\sigma = 2$. (b) $\sigma = 10$.

the Gaussian values are set as $\sigma = 2$ and 10. The blue ellipse indicates the low coherency of texture or the normal tension of roughness fluctuations, whereas red indicates data inconsistency with higher entropy as well as rapid intensity alteration known as highly textured areas. Their elliptic axes can be oriented toward a specific direction of O that shows coherency toward the surrounding cells, which signifies the local structural similarity (SSIM) among the neighboring cells. It should be noted that the cell set number selection plays an essential role in TSD field map computation. A larger number gives a better visualization result with larger ellipses, but it also reduces the precision and accuracy of the analysis, which is not good. In this study, the number is considered a group of four pixels. Similarly, the TSD synthesis results of the received backscattered data are determined under the same conditions as in Fig. 22 and are presented in Fig. 23.

The TSD map in Fig. 23(a) with $\sigma = 2$ has less harmony in the orientation and less consistency in the coherency compared to its counterpart with $\sigma = 10$ in Fig. 23(b) or the TSD field map of texture in Fig. 22(a). This shows that backscattering is more sensitive to the surface roughness, and image formation plays a key role in the focusing of noncoherent reception and texture consistency [53], [67], [70], [73]. Accordingly, roughness fluctuations play a significant role in noncoherent backscattering and the inconsistency of raw data rather than its pertinent reconstructed image. However, the role of the Gaussian factor is important in such a synthesis. As a result, in the case of CRPM texture including homogenous areas such as thick ice floes or

TABLE IV
QUANTITATIVE METRICS OF THE NORMALIZED CRPM SURFACE UNDER SEA STATE CONDITIONS [WIND DIRECTION $=12^\circ$, $\Delta = 0.1$ m, AND SPEED ALTERATIONS]

Wind speed [km/h]	9	10	11	12	13	14	15	16	17
MSE	0.81	0.74	0.71	0.73	0	0.98	1.10	1.63	1.82
MIV	0.36	0.50	0.67	0.61	0.89	0.97	1.06	1.34	1.49
Var.	0.07	0.14	0.23	0.22	0.43	0.52	0.63	0.97	1.11
SNR [dB]	17.85	16.81	15.96	17.71	16.01	16.40	16.61	15.55	16.34
PSNR [dB]	0.92	1.30	1.50	1.37	-	0.09	-0.41	-2.12	-2.59
SSIM	0.84	0.83	0.82	0.82	1	0.77	0.77	0.68	0.66

pure open water that spatially deal with the uniform changes of surface roughness, the coherency of texture is almost low, and they are oriented toward their local vectors.

However, as the magnitude of fluctuations increases at a higher rate within each principal direction, which is a sign of ice edges or undulating open water, not only will the shape of elliptic descriptors change, but their orientation and coherency will also be modified into anisotropic structures. In this case, a higher order of σ provides a smoother tension, which is quite sensitive for raw data analysis. Hence, prior to SAR image reconstruction, a nonparametric dataset synthesis consisting of geometric distortions via TSD synthesis would help reconstruct the texture closer to reality. As previously mentioned, the group number of cells will only affect the computation complexities, and the larger the number is, the lower the computational burden and the lower the accuracy. The results in Fig. 24 show how the group number changed the detailed information of the TSD synthesis of texture under the same conditions as in Fig. 22. Here, the group number is selected to be 23, which is 6 times larger than in Figs. 22 and 23. As seen in Fig. 24, the information is not as complete as expected. As a rule of thumb, it is recommended to use a low group number with a medium value of σ, which is related to the size of the texture.

IV. OBJECTIVE QUALITY ASSESSMENT VERIFICATION

Various metrics can be used for surface roughness assessment to determine how precise the CRPM roughness modeling has been performed. However, the importance of the sea state conditions on the CRPM is decisive, which makes metric selection a crucial task for texture evaluation. Hence, in this section, a quantitative objective assessment will be carried out on the simulation results under different sea state conditions and will be compared with the reference sea state conditions of 13 km/h, $\theta = 12^\circ$, and $\Delta = 0.1$ m. The objective assessment consists of pixel-based metrics such as the mean square error (MSE), signal-to-noise ratio (SNR), peak SNR (PSNR), variance, mean intensity value (MIV), SSIM index, and SSIM map. In addition, with the help of normalized cross-correlation (NCC) measurements between the reference model and other simulation results, an extended correlation-based technique that evaluates the pattern of roughness will be presented. The results of objective quality assessments are listed in Tables IV and V as well as shown in Figs. 25 and 26. It should be noted that all textures have experienced roughness fluctuations due to the

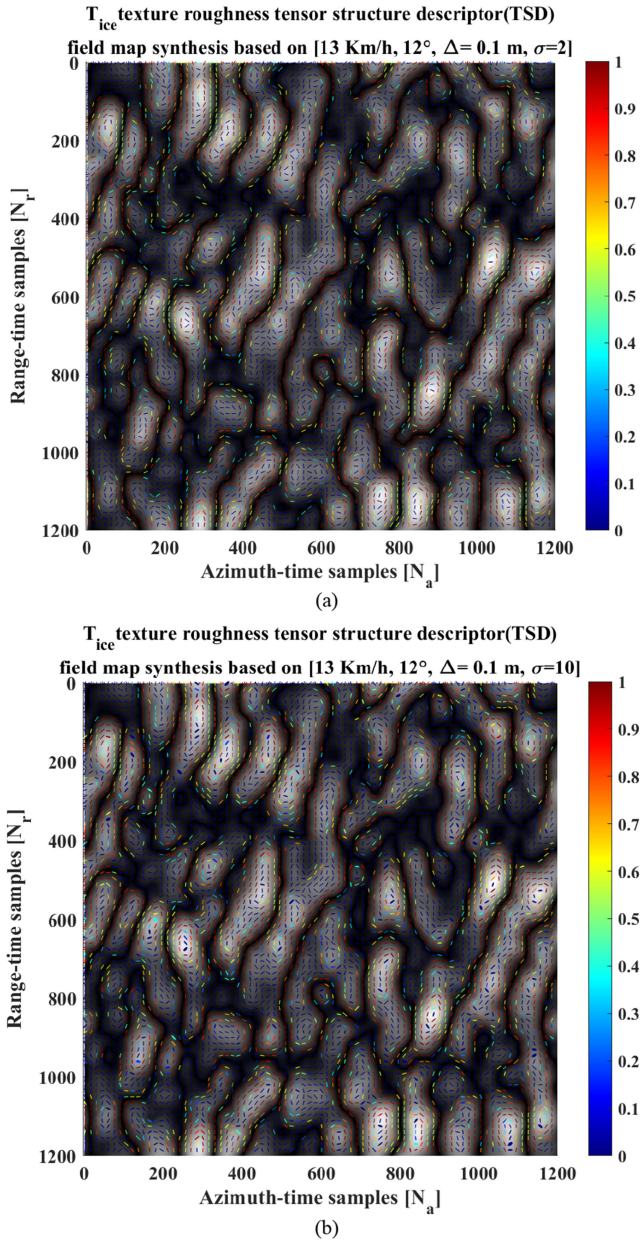

Fig. 24. CRPM surface roughness tension results based on TDS field synthesis under the reference sea state condition of wind speed = 13 km/h, $\theta = 12^\circ$, $\Delta = 0.1$ m, and pixel group of 20. (a) $\sigma = 2$. (b) $\sigma = 10$.

TABLE V
QUANTITATIVE METRICS OF THE NORMALIZED CRPM SURFACE UNDER SEA STATE CONDITIONS [SPEED = 13 KM/H, $\Delta = 0.1$ m, AND DIRECTION DEVIATIONS]

Wind direction [degree]	8	9	10	11	12	13	14	15	16
MSE	0.83	0.79	0.82	0.76	0	0.97	0.80	0.91	0.82
MIV	0.82	0.75	0.75	0.64	0.89	0.92	0.79	0.89	0.80
Var.	0.38	0.34	0.34	0.26	0.43	0.45	0.38	0.46	0.37
SNR [dB]	16.60	17.25	17.28	18.53	16.01	15.71	16.82	15.91	16.82
PSNR [dB]	0.83	1.02	0.88	1.16	-	0.12	0.97	0.40	0.88
SSIM	0.78	0.78	0.80	0.80	1	0.75	0.79	0.76	0.78

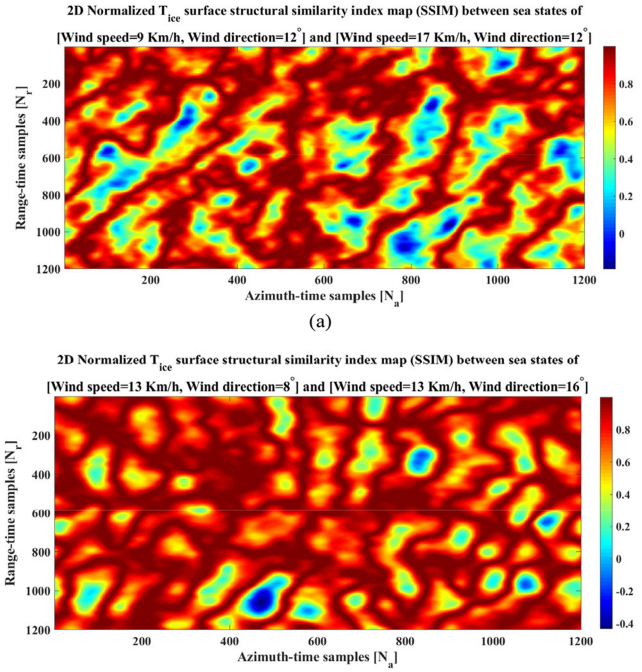

Fig. 25. CRPM surface roughness SSIM map between (a) wind speed = 9 km/h, $\theta = 12^\circ$ versus wind speed = 17 km/h and $\theta = 12^\circ$ and (b) wind speed = 13 km/h and $\theta = 8^\circ$ versus wind speed = 13 km/h and $\theta = 16^\circ$.

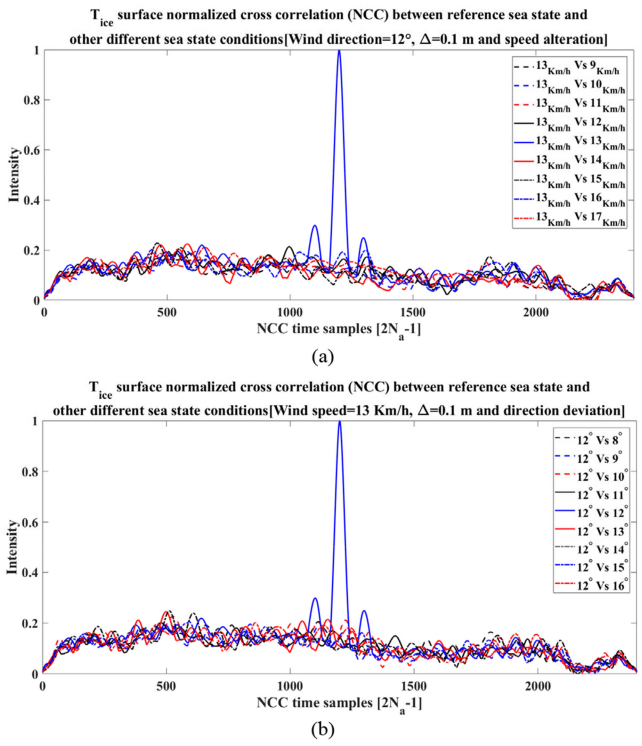

Fig. 26. CRPM surface roughness NCC comparison between different sea states and the reference speed = 13 km/h, $\theta = 12^\circ$, and $\Delta = 0.1$ m. (a) Speed alteration scenario. (b) Direction deviation scenario.

random entity of scattering components under the control of the sea state, which are investigated quantitatively here.

As seen from the metrics, the impact of change in the sea state is relativistic, and no sea state outperforms the other. Additionally, there are no limits for metrics in their domain compared to the reference condition. As seen from the results in Table IV and specifically at speed values higher than 14 km/h, MSEs are derived higher than the unit, and subsequently, their PSNRs are obtained as negative values. To explain such metric behaviors, the CRPM surface under the speed alteration scenario in Fig. 6 should be referred to, where the freeboard heights were derived to be larger than other sea state conditions at speeds higher than 14 km/h. If the resolution cell scatterings are overly affected by the sea state, which makes the entity of the spectral component change in a nonlinear manner different from the reference, then the MSE would drive larger than one unit compared to the reference. In other words, the high value of MSE indicates more significant variance in individual cells within the texture in comparison to the reference texture, which confirms that the roughness at speeds greater than 14 km/h are not structurally located on the same class as the reference image, and they can be categorized into different type based on their freeboard height. This is also true for the negative values of PSNR. These metric behaviors cannot be found in Table V in the case of wind direction deviations. As a rule of thumb, the lower the MSE is, the higher the match between textures, and the quality effects of speed alteration in metrics are much more intense than direction deviation.

As seen from the results listed above, wind direction instills small-scale changes in the texture, whereas speed alterations higher than 14 km/h instill medium-scale changes in terms of different classes of CRPM. The SSIM maps in Fig. 25 confirm the structural similarity of textures. As shown in Fig. 25(a), under the reference sea state conditions of $\theta = 12^\circ$ and $\Delta = 0.1$ m with the alteration in speed, the SSIM map between the lowest speed 9 km/h and the maximum speed 16 km/h is derived to be approximately 0.7. Meanwhile, in Fig. 25(b), under the similar reference condition of 13 km/h and $\Delta = 0.1$ m with the alteration in direction, the SSIM map between the lowest direction of 8° and the maximum direction 16° is derived to be approximately 0.8, which shows the rate of similarity. This also shows that under the speed alteration scenario, the ice floes have the least structural similarity due to their orientations and structures, which is a medium-scale effect.

The results are almost different in the direction deviation scenario, and ice floes mostly present small-scale structures in a similar manner. The simulation results in Fig. 26 are also true for other roughness evaluation scenario under different sea state conditions. Fig. 26 shows the NCC value between the reference roughness modeling and other sea state modelings. As seen in Fig. 26(a) and (b), roughness under different sea state conditions not only lack structural similarity to the reference condition, but each texture is entirely different from the other modeling. In short, each sea state condition leads to energy scattering in the form of specific spectral components, which leads to distinct coupling effects and textures that belong to a particular class of surface roughness.

V. Conclusion

In view of the importance of polar regions and their impact on global climate change, there is an urgent need for a reliable polar media modeling. Such a modeling will provide data for the generation of the medium and the formation and melting of its structures due to ocean wave interactions. However, to date, most models have ignored the role of ocean waves in the modulation processes, and their wavefield scattering in the presence of ice floes do not specifically describe the problem of roughness under sea state conditions. In this research, these processes are studied in terms of CRPM energy scattering functions by using a modified version of the JONSWAP formulation, which is finally visualized in the form of a CRPM surface roughness model. The main approach of this study is the modification of the JONSWAP formulation based on an optimized cosine-power gamma PDF application under the control of the sea state along with roughness smoothing, which comprises two-scale approach of statistical CRPM surface modeling. The two-scale model, known as the composite model, is widely applied to describe the directional wave spectrum and its contribution to radar observations but suffers from spectrum computational complexities. Accordingly, a parallel processing technique has been adopted for the optimized computation and extraction of ice energy function.

The results obtained from the parallel processing of CRPM modeling carried out under the designated sea state condition paved the way for simulating sea ice textures under different sea states, including wind speed alterations and direction deviations, known as fractal visualization. From the results of fractal texture, it is deduced that some of the reference input energy is modified or lost in different modes as a function of sea state, while the waves are redistributed with different rates and magnitudes. As those modified waves travel further along the fetch, their wavenumber changes, and likewise, the shapes of floes and their orientation change, which is under the control of wind speed and direction. However, the speed alteration plays a major role in the origination of CRPM rather than the direction.

The results also show that the sea state directly affects the composite structure of CRPM so that low-frequency components act as narrowband filters for ocean waves, whereas high-frequency components proceed as wideband modulations that have a major contribution to roughness fluctuations. Accordingly, regions of roughness fluctuations, known as highly textured areas, which are sensitive to sea state conditions, are considered for further texture investigation. The investigation includes PSD formulation and the simulation of the highly textured area as well as their electromagnetic interaction evaluation in terms of RDG, both in a hybrid domain. For further surface texture analysis, a nonparametric texture synthesis for surface tension in terms of TSD was also applied. The obtained results of PSD, RDG, and TSD show their capacity to synthesize different textures of CRPM and prove that the proposed CRPM modeling method, in addition to its evaluations, works correctly in terms of composite structures.

Additionally, to evaluate the quality of numerical modeling, an objective quality assessment was used along with the above-mentioned items. The obtained results are highly compliant with the modeling results and prove that the proposed statistical method of two-scale CRPM roughness modeling is in compliance with the theory and formulations. The proposed approach appears to be faster when the parallel processing method is used.

Although brief, this research, together with the extensive references, can hopefully help readers obtain a comprehensive view of the evolution of the CRPM. There are several critical future improvements required, which are listed as follows:

1) study the source terms of wind input, dissipation, and nonlinear interaction for ocean waves in the modeling of CRPM based on different scattering functions;
2) derive a governing equation for energy scattering to be implemented into a global ocean wave model;
3) apply the inverse method to estimate the physical parameters in viscoelastic models from laboratory and field data;
4) conduct roughness tension analysis based on other domains of validity.

Hence, we expect the continuation of this study to provide answers to further questions in terms of spectral energy, sea states, energy balance, and composite behaviors, which are helpful for microwave radiometry, temperature profile derivation, band fusion, and other applications.

Acknowledgment

The authors would like to thank the Korea Polar Research Institute for providing all facilities for this research.

References

[1] L. A. Roach, C. Horvat, S. M. Dean, and C. M. Bitz, "An emergent sea ice floe size distribution in a global coupled ocean-sea ice model," *J. Geophys. Res., Oceans*, vol. 123, no. 6, pp. 4322–4337, Jun. 2018.

[2] Q. Zhang and R. Skjetne, "Image processing for identification of sea-ice floes and the floe size distributions," *IEEE Trans. Geosci. Remote Sens.*, vol. 53, no. 5, pp. 2913–2924, May 2015.

[3] F. Montiel, V. A. Squire, and L. G. Bennetts, "Attenuation and directional spreading of ocean wave spectra in the marginal ice zone," *J. Fluid Mech.*, vol. 790, pp. 492–522, Feb. 2016.

[4] Z. Wang *et al.*, "Multichannel wideband synthetic aperture radar for ice sheet remote sensing: Development and the first deployment in Antarctica," *IEEE J. Sel. Topics Appl. Earth Observ. Remote Sens.*, vol. 9, no. 3, pp. 980–993, Mar. 2016.

[5] L. A. Roach, M. M. Smith, and S. M. Dean, "Quantifying growth of pancake sea ice floes using images from drifting buoys," *J. Geophys. Res., Oceans*, vol. 123, no. 4, pp. 2851–2866, Apr. 2018.

[6] C. O. Collins, III, W. E. Rogers, A. Marchenko, and A. V. Babanin, "In situ measurements of an energetic wave event in the Arctic marginal ice zone," *Geophys. Res. Lett.*, vol. 42, no. 6, pp. 1863–1870, Mar. 2015.

[7] F. Montiel and V. A. Squire, "Modelling wave-induced sea ice break-up in the marginal ice zone," *Proc. Roy. Soc. A, Math., Phys. Eng. Sci.*, vol. 473, no. 2206, Oct. 2017, Art. no. 20170258.

[8] V. A. Squire and F. Montiel, "Evolution of directional wave spectra in the marginal ice zone: A new model tested with legacy data," *J. Phys. Oceanogr.*, vol. 46, no. 10, pp. 3121–3137, Oct. 2016.

[9] A. L. Kohout and M. H. Meylan, "An elastic plate model for wave attenuation and ice floe breaking in the marginal ice zone," *J. Geophys. Res.*, vol. 113, no. C9, Sep. 2008, Art. no. C09016.

[10] M. H. Meylan and D. Masson, "A linear Boltzmann equation to model wave scattering in the marginal ice zone," *Ocean Model.*, vol. 11, no. 3/4, pp. 417–427, Jan. 2006.

[11] A. L. Kohout and M. H. Meylan, "A model for wave scattering in the marginal ice zone based on a two-dimensional floating-elastic-plate solution," *Ann. Glaciol.*, vol. 44, pp. 101–107, 2006.

[12] L. Hermozo, L. Eymard, and F. Karbou, "Modeling sea ice surface emissivity at microwave frequencies: Impact of the surface assumptions and potential use for sea ice extent and type classification," *IEEE Trans. Geosci. Remote Sens.*, vol. 55, no. 2, pp. 943–961, Feb. 2017.

[13] P. Sutherland and J. Gascard, "Airborne remote sensing of ocean wave directional wavenumber spectra in the marginal ice zone," *Geophys. Res. Lett.*, vol. 43, no. 10, pp. 5151–5159, May 2016.

[14] R. Dusséaux, S. Afifi, and M. Dechambre, "Scattering properties of a stratified air/snow/sea ice medium. Small slope approximation," *Comptes Rendus Physique*, vol. 17, no. 9, pp. 995–1002, Nov. 2016.

[15] G. L. Vaughan and V. A. Squire, "Ocean wave scattering by natural sea ice transects," *J. Geophys. Res.*, vol. 113, no. C10, Oct. 2008, Art. no. C10022.

[16] M. H. Meylan and L. G. Bennetts, "Three-dimensional time-domain scattering of waves in the marginal ice zone," *Philos. Trans. Roy. Soc. A, Math., Phys. Eng. Sci.*, vol. 376, no. 2129, Aug. 2018, Art. no. 20170334.

[17] F. Ardhuin, P. Sutherland, M. Doble, and P. Wadhams, "Ocean waves across the Arctic: Attenuation due to dissipation dominates over scattering for periods longer than 19s," *Geophys. Res. Lett.*, vol. 43, no. 11, pp. 5775–5783, Jun. 2016.

[18] K. M. Golden *et al.*, "Forward electromagnetic scattering models for sea ice," *IEEE Trans. Geosci. Remote Sens.*, vol. 36, no. 5, pp. 1655–1674, Sept. 1998.

[19] X. Zhao, H. H. Shen, and S. Cheng, "Modeling ocean wave propagation under sea ice covers," *Acta Mechanica Sinica*, vol. 31, no. 1, pp. 1–15, Feb. 2015.

[20] X. Zhao and H. Shen, "A diffusion approximation for ocean wave scatterings by randomly distributed ice floes," *Ocean Model.*, vol. 107, pp. 21–27, Nov. 2016.

[21] P. Sutherland, J. Brozena, W. E. Rogers, M. Doble, and P. Wadhams, "Airborne remote sensing of wave propagation in the marginal ice zone," *J. Geophys. Res.. Oceans*, vol. 123, no. 6, pp. 4132–4152, Jun. 2018.

[22] D. Monteban, H. Johnsen, and R. Lubbad, "Spatiotemporal observations of wave dispersion within sea ice using sentinel-1 SAR TOPS mode," *J. Geophys. Res., Oceans*, vol. 124, no. 12, pp. 8522–8537, Dec. 2019.

[23] K. F. Warnick and W. C. Chew, "Numerical simulation methods for rough surface scattering," *Waves Random Media*, vol. 11, no. 1, pp. R1–R30, Jan. 2001.

[24] G. Wu, J. Fan, F. Zhang, and F. Lu, "A semi-empirical model of sea clutter based on zero memory nonlinearity," *IEEE Access*, vol. 7, pp. 18125–18137, 2019.

[25] V. A. Ruiz-Cortés and J. C. Dainty, "Experimental light-scattering measurements from large-scale composite randomly rough surfaces," *J. Opt. Soc. Amer. A*, vol. 19, no. 10, Oct. 2002, Art. no. 2043.

[26] Y. Liu, Z. Yao, and H. Li, "Analytical and experimental studies on hydrodynamic performance of semi-immersed Jarlan-type perforated breakwaters," *China Ocean Eng.*, vol. 29, no. 6, pp. 793–806, Nov. 2015.

[27] Y. Yang, W. Luo, B. Yin, and Y. Ren, "Electromagnetic scattering of rough ground surface covered by multilayers vegetation," *Int. J. Antennas Propag.*, vol. 2019, pp. 1–12, Apr. 2019.

[28] Y. Kuga, C. T. C. Le, A. Ishimaru, and L. Ailes-Sengers, "Analytical, experimental, and numerical studies of angular memory signatures of waves scattered from one-dimensional rough surfaces," *IEEE Trans. Geosci. Remote Sens.*, vol. 34, no. 6, pp. 1300–1307, Nov. 1996.

[29] T. Nordam, P. A. Letnes, and I. Simonsen, "Numerical simulations of scattering of light from two-dimensional rough surfaces using the reduced Rayleigh equation," *Front. Phys.*, vol. 1, 2013, Art. no. 8.

[30] Y. Liang, X. H. Zeng, L. X. Guo, and Z. S. Wu, "Review on the pre-study about specific target and rough soil surface composite electromagnetic scattering basing on an efficient numerical strategy," in *Proc. Prog. Electromagn. Res. Symp.*, Aug. 2016, pp. 3198–3198.

[31] J. T. Johnson, "A numerical study of scattering from an object above a rough surface," *IEEE Trans. Antennas Propag.*, vol. 50, no. 10, pp. 1361–1367, Oct. 2002.

[32] J. V. Toporkov and G. S. Brown, "Numerical simulations of scattering from time-varying, randomly rough surfaces," *IEEE Trans. Geosci. Remote Sens.*, vol. 38, no. 4, pp. 1616–1625, Jul. 2000.

[33] S. T. McDaniel, "Geometrical optics prediction of surface scattering statistics," *IEEE Trans. Geosci. Remote Sens.*, vol. 42, no. 2, pp. 361–366, Feb. 2004.

[34] H. Chen, M. Zhang, and H.-C. Yin, "Facet-based treatment on microwave bistatic scattering of three-dimensional sea surface with electrically large ship," *Prog. Electromagn. Res.*, vol. 123, pp. 385–405, 2012.

[35] E. A. Karjadi, M. Badiey, J. T. Kirby, and C. Bayindir, "The effects of surface gravity waves on high-frequency acoustic propagation in shallow water," *IEEE J. Ocean. Eng.*, vol. 37, no. 1, pp. 112–121, Jan. 2012.

[36] O. Ozgun and M. Kuzuoglu, "Monte Carlo-based characteristic basis finite-element method (MC-CBFEM) for numerical analysis of scattering from objects on/above rough sea surfaces," *IEEE Trans. Geosci. Remote Sens.*, vol. 50, no. 3, pp. 769–783, Mar. 2012.

[37] N. Choi and J. E. Harvey, "Numerical validation of the generalized Harvey–Shack surface scatter theory," *Opt. Eng.*, vol. 52, no. 11, Nov. 2013, Art. no. 115103.

[38] C. Kanu and R. Snieder, "Numerical computation of the sensitivity kernel for monitoring weak changes with multiply scattered acoustic waves," *Geophys. J. Int.*, vol. 203, no. 3, pp. 1923–1936, Nov. 2015.

[39] Q. Liu, A. Babanin, Y. Fan, S. Zieger, C. Guan, and I.-J. Moon, "Numerical simulations of ocean surface waves under hurricane conditions: Assessment of existing model performance," *Ocean Mode.*, vol. 118, pp. 73–93, Oct. 2017.

[40] Y. Demarty, L. Thirion-Lefevre, and V. Gobin, "Modelling of the electromagnetic scattering by sea surfaces at grazing incidence. Application to HF surface wave radars," *Comptes Rendus Physique*, vol. 11, no. 1, pp. 87–95, Jan. 2010.

[41] A. A. Mouche, B. Chapron, and N. Reul, "A simplified asymptotic theory for ocean surface electromagnetic wave scattering," *Waves Random Complex Media*, vol. 17, no. 3, pp. 321–341, Jun. 2007.

[42] P.-B. Wei, M. Zhang, D. Nie, and Y.-C. Jiao, "Statistical realisation of CWMFSM for scattering simulation of space-time varying sea surface," *Int. J. Remote Sens.*, vol. 40, no. 1, pp. 332–345, Sep. 2018.

[43] H. Pan, W. Zhang, W. Jiang, P. Wang, J. Yang, and X. Zhang, "Roughness change analysis of sea surface from visible images by fractals," *IEEE Access*, vol. 8, pp. 78519–78529, 2020.

[44] M. T. Silva, W. Huang, and E. W. Gill, "High-frequency radar cross-section of the ocean surface with arbitrary roughness scales: A generalized functions approach," *IEEE Trans. Antennas Propag.*, vol. 69, no. 3, pp. 1643–1657, Mar. 2021.

[45] H. Pan, P. Gao, H. Zhou, R. Ma, J. Yang, and X. Zhang, "Roughness analysis of sea surface from visible images by texture," *IEEE Access*, vol. 8, pp. 46448–46458, 2020.

[46] D. Chalikov, "Numerical modeling of surface wave development under the action of wind," *Ocean Sci.*, vol. 14, no. 3, pp. 453–470, Jun. 2018.

[47] V. A. Squire, "Past, present and impendent hydroelastic challenges in the polar and subpolar seas," *Philos. Trans. Roy. Soc. A, Math., Phys. Eng. Sci.*, vol. 369, no. 1947, pp. 2813–2831, Jul. 2011.

[48] V. A. Squire, "A fresh look at how ocean waves and sea ice interact," *Philos. Trans. Roy. Soc. A, Math., Phys. Eng. Sci.*, vol. 376, no. 2129, Aug. 2018, Art. no. 20170342.

[49] I. H. Shahrezaei, H.-C. Kim, and T.-B. Chae, "Ultra-high resolution KOMPSAT-5 SAR sea-ice random radiometric anomaly formulation based on hybrid domain texture decomposition," in *Proc. Int. Conf. Radar, Antenna, Microw., Electron., Telecommun.*, 2020, pp. 325–330.

[50] J. Park, J. Won, A. A. Korosov, M. Babiker, and N. Miranda, "Textural noise correction for sentinel-1 TOPSAR cross-polarization channel images," *IEEE Trans. Geosci. Remote Sens.*, vol. 57, no. 6, pp. 4040–4049, Jun. 2019.

[51] J. Park, A. A. Korosov, M. Babiker, S. Sandven, and J. Won, "Efficient thermal noise removal for sentinel-1 TOPSAR cross-polarization channel," *IEEE Trans. Geosci. Remote Sens.*, vol. 56, no. 3, pp. 1555–1565, Mar. 2018.

[52] J. C. Landy, M. Tsamados, and R. K. Scharien, "A Facet-based numerical model for simulating SAR altimeter echoes from heterogeneous sea ice surfaces," *IEEE Trans. Geosci. Remote Sens.*, vol. 57, no. 7, pp. 4164–4180, Jul. 2019.

[53] I. Heidarpour Shahrezaei and H. Kim, "Fractal analysis and texture classification of high-frequency multiplicative noise in SAR sea-ice images based on a transform-domain image decomposition method," *IEEE Access*, vol. 8, pp. 40198–40223, 2020.

[54] N. Pinel, B. Chapron, C. Bourlier, N. de Beaucoudrey, R. Garello, and A. Ghaleb, "Statistical analysis of real aperture radar field backscattered from sea surfaces under moderate winds by Monte Carlo simulations," *IEEE Trans. Geosci. Remote Sens.*, vol. 52, no. 10, pp. 6459–6470, Oct. 2014.

[55] J. Li, M. Zhang, W. Fan, and D. Nie, "Facet-based investigation on microwave backscattering from sea surface with breaking waves: Sea spikes and SAR imaging," *IEEE Trans. Geosci. Remote Sens.*, vol. 55, no. 4, pp. 2313–2325, Apr. 2017.

[56] E. M. Nassar, J. T. Johnson, and R. Lee, "A numerical model for electromagnetic scattering from sea ice," *IEEE Trans. Geosci. Remote Sens.*, vol. 38, no. 3, pp. 1309–1319, May 2000.

[57] D. Zahn, K. Sarabandi, K. F. Sabet, and J. F. Harvey, "Numerical simulation of scattering from rough surfaces: A wavelet-based approach," *IEEE Trans. Antennas Propag.*, vol. 48, no. 2, pp. 246–253, Feb. 2000.

[58] F. Pérez-Ràfols and A. Almqvist, "Generating randomly rough surfaces with given height probability distribution and power spectrum," *Tribol. Int.*, vol. 131, pp. 591–604, Mar. 2019.

[59] B. Liu and Y. He, "SAR raw data simulation for ocean scenes using inverse omega-K algorithm," *IEEE Trans. Geosci. Remote Sens.*, vol. 54, no. 10, pp. 6151–6169, Oct. 2016.
[60] J. A. Ogilvy and H. M. Merklinger, "Theory of wave scattering from random rough surfaces," *J. Acoust. Soc. Amer.*, vol. 90, no. 6, pp. 3382–3382, Dec. 1991.
[61] D. Masson and P. H. Leblond, "Spectral evolution of wind-generated surface gravity waves in a dispersed ice field," *J. Fluid Mech.*, vol. 202, pp. 43–81, May 1989.
[62] S. Hamran and E. Aarholt, "Glacier study using wavenumber domain synthetic aperture radar," *Radio Sci.*, vol. 28, no. 4, pp. 559–570, Jul./Aug. 1993.
[63] I. Heidarpour Shahrezaei, M. Kazerooni, and M. Fallah, "A complex target terrain SAR raw data generation and evaluation based on inversed equalized hybrid-domain algorithm processing," *Waves Random Complex Media*, vol. 27, no. 1, pp. 47–66, Jun. 2016.
[64] Y. Du, *Electromagnetic Scattering: A Remote Sensing Perspective*. Hackensack, NJ, USA: World Scientific, 2017.
[65] T. Elfouhaily, B. Chapron, K. Katsaros, and D. Vandemark, "A unified directional spectrum for long and short wind-driven waves," *J. Geophys. Res., Oceans*, vol. 102, no. C7, pp. 15781–15796, Jul. 1997.
[66] M. Al-Ani and M. Belmont, "On fully describing the probability distribution of quiescent periods from sea spectral density," *IEEE J. Ocean. Eng.*, vol. 46, no. 1, pp. 143–155, Jan. 2021.
[67] J. Prendergast, M. Li, and W. Sheng, "A study on the effects of wave spectra on wave energy conversions," *IEEE J. Ocean. Eng.*, vol. 45, no. 1, pp. 271–283, Jan. 2020.
[68] T. W. Dixon and V. A. Squire, "Energy transport velocity of flexural waves in a random medium," *Waves Random Media*, vol. 10, no. 1, pp. 83–102, Jan. 2000.
[69] T. W. Dixon and V. A. Squire, "Energy transport in the marginal ice zone," *J. Geophys. Res., Oceans*, vol. 106, no. C9, pp. 19917–19927, Sep. 2001.
[70] I. H. Shahrezaei and H. Kim, "Resolutional analysis of multiplicative high-frequency speckle noise based on SAR spatial de-Speckling filter implementation and selection," *Remote Sens.*, vol. 11, no. 9, May 2019, Art. no. 1041.
[71] M. Ivanovici, "Fractal dimension of color fractal images with correlated color components," *IEEE Trans. Image Process.*, vol. 29, pp. 8069–8082, Jul. 2020.
[72] I. H. Shahrezaei, M. Kazerooni, and M. Fallah, "A total quality assessment solution for synthetic aperture radar NLFM waveform generation and evaluation in a complex random media," *Int. J. Smart Sens. Intell. Syst.*, vol. 10, no. 1, pp. 174–198, 2017.
[73] A. Akl, C. Yaacoub, M. Donias, J. D. Costa, and C. Germain, "Texture synthesis using the structure tensor," *IEEE Trans. Image Process.*, vol. 24, no. 11, pp. 4082–4095, Nov. 2015.
[74] R. Pike and P. Sabatier, *Scattering: Scattering and Inverse Scattering in Pure and Applied Science*. New York, NY, USA: Academic, 2001.
[75] J. A. Johannessen *et al.*, "Coastal ocean fronts and eddies imaged with ERS 1 synthetic aperture radar," *J. Geophys. Res., Oceans*, vol. 101, no. C3, pp. 6651–6667, Mar. 1996.
[76] Z. Zhu, H. Zhang, and F. Xu, "Raw signal simulation of synthetic aperture radar altimeter over complex terrain surfaces, " *Radio Sci.*, vol. 55, no. 2, pp. 1–17, Feb. 2020.
[77] P. Wadhams, V. A. Squire, J. A. Ewing, and R. W. Pascal, "The effect of the marginal ice zone on the directional wave spectrum of the ocean," *J. Phys. Oceanogr.*, vol. 16, no. 2, pp. 358–376, Feb. 1986.
[78] E. M. Schulson, "Friction of sea ice," *Philos. Trans. Roy. Soc. A.*, vol. 376, no. 2129, Aug. 2018, Art. no. 20170336.
[79] K. Hasselmann, "On the non-linear energy transfer in a gravity-wave spectrum part 1. General theory," *J. Fluid Mech.*, vol. 12, no. 4, pp. 481–500, Apr. 1962.
[80] L. Tsang and J. A. Kong, *Scattering of Electromagnetic Waves: Advanced Topics*. Hoboken, NJ, USA: Wiley, 2001.

Iman Heidarpour Shahrezaei was born in Isfahan, Iran, in 1985. He received the B.Sc. and M.Sc. degrees in electrical and telecommunication engineering (waves and fields) from the University of Urmia, Urmia, Iran, in 2007 and 2011, respectively, and the Ph.D. degree in electrical and telecommunication engineering (waves and fields) from the Malek-Ashtar University of Technology, Tehran, Iran, in 2017.

Since December 2018, he has been a Postdoctoral Researcher with the Center for Remote Sensing and Geospatial Information Systems, Korea Polar Research Institute, Incheon, South Korea. The center consists of numerical data analysis and satellite signal modeling. His current research interests include radar remote sensing, microwave imaging, modeling in remote sensing, image analysis and data fusion, radiation modeling, backscattering theories as well as the development of image formation algorithms.

Hyun-Cheol Kim (Member, IEEE) received the Ph.D. degree in earth and environmental sciences with a major in satellite oceanography from Seoul National University, Seoul, South Korea, in 2006.

Since 2007, he has been with the Korea Polar Research Institute (KOPRI), Incheon, South Korea, using satellite and unmanned aerial vehicle (UAV) remote sensing data for the purpose of Arctic and Antarctic research. He established a remote sensing group in KOPRI in 2016. He leads the Center for Remote Sensing and GIS as the Director. The center consists of many specialized fields of satellite remote sensing, ocean color, synthetic aperture radar (SAR), passive microwave, optical remote sensing, and UAVs. The group mainly studies the cryosphere for climate change using remote sensing data. Notably, he is the first scientist to use Korea Multipurpose Satellite (KOMPSAT) for polar science. He is also actively involved in many international programs.

Dr. Kim was a recipient of a Korea Prime Ministerial Citation for Excellence in Ocean Science in 2019.